



Partenaire stratégique
Institut Mines-Télécom

Université de Strasbourg

TOUCHTE CODJO Felix
Promotion **2024**
Année universitaire **2023-2024**

Diplôme d'ingénieur Télécom Physique Strasbourg

Mémoire de stage de 3^e année

Préparation de l'expérience ALERT au laboratoire Jefferson

Du 01 Mars 2024 au 15 Août 2024

Tuteur : Raphaël Dupré
raphael.dupre@ijclab.in2p3.fr



Remerciements

Le présent rapport de stage est l'aboutissement d'une année scolaire riche en émotions. Cette année, j'ai reçu une merveilleuse leçon d'humilité, moi pour qui tout réussissait normalement. Cette année, j'ai pris connaissance des limites de ma méthode de travail. Cette année, j'ai appris à demander de l'aide.

Ma conception de la réussite était trop exigeante et j'avais failli perdre tous mes moyens lorsque les choses ne se passaient pas comme prévu. Par chance, j'ai pu bénéficier du soutien qu'il fallait aux moments opportuns.

Je tiens à remercier Boris Hippolyte du master PSA qui m'a toujours reçu dans son bureau pour discuter de sujets variés : carrière scientifique, interprétation des résultats scolaires, enseignements de la vie.

Je remercie également Anne-Sophie Cordan et Yann Leroy de Télécom Physique Strasbourg qui ont su m'encourager et soutenir ma candidature à la thèse que je réaliserai au sein de l'IJCLab dès le mois d'octobre 2024.

Enfin, je tiens à remercier, mon tuteur de stage, Raphaël Dupré, pour m'avoir donné l'opportunité de réaliser mon projet de fin d'étude d'ingénieur au sein de son équipe de recherche à l'IJCLab.

Contents

Introduction	1
1 Hosting organization	2
1.1 Overview	2
1.2 Structure	3
2 Physics motivation	6
2.1 Nucleon structure	6
2.1.1 Deep inelastic scattering	6
2.1.2 Generalized parton distributions	8
2.1.3 EMC effect	10
2.2 Proposed measurement	10
2.2.1 DVCS	11
2.2.2 Tagged EMC	11
3 ALERT at Jefferson Lab	13
3.1 CEBAF	13
3.2 CLAS12	13
3.3 ALERT	14
3.3.1 AHDC	16
3.3.2 ATOF	16
4 ALERT Simulation	19
4.1 Presentation	19
4.2 Digitization	20
4.2.1 Event in GEMC	20
4.2.2 Drift time calculation	22
4.2.3 Signal generation	26
4.3 Decoding	29
4.4 Analysis	32

Conclusion	39
A Appendix	40
A.1 Doca calculation	40
A.2 Reconstruction	41
Bibliography	43

List of Figures

1.1	Key figures of IJCLab. Source [1].	4
1.2	IJCLab organization chart. Source [2].	5
2.1	The Feynman diagram of a deep inelastic scattering at leading order. A virtual photon γ^* carries the exchanged four-momentum q . k , k' and p are respectively the four-momenta of the incoming lepton, the outgoing lepton and the target nucleon.	7
2.2	Parton distribution functions of the proton obtained by MMHT2014 Next to Next to leading order PDFs at $Q^2 = 10 \text{ GeV}^2$ and $Q^2 = 10^4 \text{ GeV}^2$, with associated 68 % confidence-level uncertainty band. Source [5].	8
2.3	General representation of the GPDs of a nucleon represented by the triple line and noted N. Single lines represent quarks or anti-quarks probed in the nucleon. Source [6, p. 6].	9
2.4	Illustration of form factors (left), parton distribution functions (center) and generalized parton distributions (right). Source [7, p. 91]	9
2.5	Ratio of the $\mathcal{F}_2^{IRON}(x, Q^2)$ structure function of iron over the $\mathcal{F}_2^{D_2}(x, Q^2)$ of deuterium. Source [10].	10
2.6	Feynman diagram of a DVCS. Source [6, p. 8].	11
2.7	The process $A(e, e'(A - 1))X$ within the impulse approximation. Source [11, p. 13].	12
3.1	(Left) Aerial view of the Jefferson Laboratory. The CEBAF continuous electron beam accelerator is represented. The dashed lines indicates the location of the accelerator, and the circle indicates the location of three experimental halls. (Right) Schematic view of the CEBAF. The linacs are represented by the arrangement of cryomodules. The letters A,B,C,D represents the four experimental halls. Source [13, 14].	14

3.2	The CLAS12 spectrometer in Hall-B. The central detectors are contained in the solenoid magnet. The other detectors constituted the forward part of CLAS12. Source [15, p. 30].	15
3.3	3D view and cutting plan of the layout of the ALERT detector. Source [16, p. 50].	16
3.4	Wires disposition of the drift chamber of ALERT. A detection cell is highlighted. It is composed a sense wire surrounded by eight field wires . A potential difference is established between the sense (+) and the field (-) wires to ensure the drift of the electrons created by ionization after the passage of a charged particle. It remains to process the signal collected by the sense wire to determine the position of the particle (see chapter 4).	17
3.5	Picture of the drift chamber of ALERT taken on the premises of IJCLab. On the left, the light of two cell phones is reflected by the sense wires of each super-layers. The 20° (from -10° to $+10^\circ$) stereo angles between the wires is clearly visible.	17
3.6	Picture of the time-of-flight system of ALERT taken on the premises of ANL. The ATOF is fixed at a cart tube.	18
4.1	(Left) Drift trajectory of electrons in ALERT for a potential difference of 1.5 kV between the wires in a 5 T magnetic field. The sense wire is at the center and is surrounded by eight field wires. Each cross is 5 ns apart. (Right) The corresponding isochronous map. Two electrons generated on the same isochronous (closed curve) will reach the sense wire at the same time. Source [16, p. 64].	20
4.2	Mechanism that leads to the signal measured by the drift chamber of ALERT.	21
4.3	Signal measured on beam at ALTO by four sense wires during the passage of an α particle of 344 MeV/c. In the first one, no particle passed in AHDC, so the electronics only measured the noise. In the last three, a signal characteristic of an electronic avalanche has been measured due to the passage of a particle in the sensing area. Source [16, p. 94].	21
4.4	Momentum distribution of initial protons generated over ten thousands events in GEMC.	22
4.5	(Left) AHDC-like cells with exaggerated concavity for easier visualisation. (Right) A set of steps (calculated in the same detection cell. The green line represents the trajectory of a particle.	23

4.6	Distribution of energy deposited, <code>geant4</code> time, r position and z position of a particular <code>MHit</code> object. This <code>MHit</code> contains 15 steps.	23
4.7	Display of the drift time associated with the signal	24
4.8	(Left) Drift time of primary electrons as a function their initial distance to the wire for various gaseous mixtures. The potential difference is still 1.5 kV, the drift chamber being in a 5 T magnetic field. (Right) Estimation of the spatial resolution of the detector as a function of the distance to the step. Source [16].	25
4.9	Distance of closest approach (doca). H_{abh} is the doca.	25
4.10	The energy deposited in each steps as a function of the drift time.	26
4.11	Simulation of the AHDC signal : before summing all Landau distributions. The distributions have been multiplied by 1000 for a better view. The time window, the delay and the scale parameter of the Landau distributions as been chosen to fit the result of the figure 4.3.	27
4.12	Simulation of the AHDC signal : after summing all Landau distributions.	27
4.13	Simulation of the electronics noise. Each point represents a sample, a draw of $\mathcal{N}(300, 30)$	28
4.14	Simulation of the AHDC signal : final result. This figure must be compare to the on-beam measurement of the figure 4.3. . .	28
4.15	Diagram of the framework used to simulate the AHDC signal. One can play with all the mentioned setting parameters to improve the results of the simulation but also with the scale parameter of the Landau distribution.	30
4.16	Decoding of the AHDC signal of the figure 4.14.	30
4.17	Example of a saturated signal.	31
4.18	Process to extract the time using the Constant Fraction Discriminator. Source [17].	33
4.19	Application of the CFD on the signal of the figure 4.16.	33
4.20	Very exotic signals. The last one is a very rare case that contributes to distorting the calculations.	34
4.21	Structure of a HIPO file.	35
4.22	Histograms of the decoding outputs.	36
4.23	Correlation between <code>t_start</code> , <code>t_cfd</code> and <code>mctime</code>	37
4.24	Correlations between the amplitude and the decoding quality. .	38

Introduction

ALERT stands for **a** low energy recoil **t**agger. It is a gaseous detector composed of a drift chamber for particle tracking and an array of scintillator for the measure of the time-of-flight. ALERT refers to a hadronic physics experiment conducted by teams of IJCLab¹ (France), ANL² (USA) and JLab³ (USA). Combined with the facilities of the Jefferson laboratory, the experiment aims to determine the nuclear structure of the ⁴He and ²H. The data will challenge various theoretical models that try to describe nuclei in terms of quarks and gluons. The data taking of the experiment is planned in February 2025.

An important part of any modern detector project is the development of its associated software. An important part of the software is the conversion of raw data from detector to human-readable data. Among other processes, it includes decoding and reconstruction. A good simulation of the response of the ALERT detector is required to write efficient and robust algorithms. The implementation of the ALERT signal generation in simulation is the main purpose of this internship.

The chapter 1 gives a presentation of the hosting organization, IJCLab. The chapter 2 presents the physics motivation for the ALERT experiment. It reviews the formalism for describing the nucleon structure and presents some measurements proposed for the detector. The chapter 3 describes the experimental setup and a description of the components of ALERT is presented. Finally, the chapter 4 presents my results on simulations carried out on the ALERT drift chamber.

¹IJCLab: Irène Joliot-Curie Laboratory

²ANL: Argonne National Laboratory

³JLab: Jefferson Laboratory

Chapter 1

Hosting organization

This internship was carried out in the "Laboratoire de physique des deux infinies Irène Joliot-Curie" (Laboratory of the Physics of the two Infinities Irène Joliot-Curie) or IJCLab. IJCLab is a joint research unit of the "Centre national de la recherche scientifique" (CNRS), Université Paris-Saclay and Université Paris-Cité, located on the Orsay campus, in France. This chapter gives a very short description of my hosting organization.

1.1 Overview

IJCLab was created in 2020 through the merger of five geographically, historically and disciplinarily close laboratories : the "Centre de spectrométrie nucléaire et de spectrométrie de masse" (CSNSM), the "Institut de physique nucléaire d'Orsay" (IPNO), the "Laboratoire de l'accélérateur linéaire" (LAL), the "Laboratoire de physique théorique" (LPT) and the unit of "Imagerie et Modélisation en Neurobiologie et Cancérologie" (IMNC). IJCLab was named in honor of Irène Juliet-Curie, winner of the Nobel Prize for Chemistry in 1935 and co-founder of the IPNO in 1956.

IJCLab employs over 730 people, including researchers, professors, engineers, technicians, PhD students and post-docs. (figure 1.1). Its activities focus on the physics of the two infinities and their applications. The laboratory aims to unravel the mysteries of matter, energy, space, time, and to understand the constituents of matter, their interactions and the origin and the evolution of the universe. As indicated in [1], the IJCLab manifesto contains :

- Leading and contributing to projects at all stages in high-energy physics, nuclear physics, astroparticles and cosmology (proposal, design, construction, operation, data analysis) with significant theory support.

- Playing a major role in the conception, design and construction of current and future accelerators.
- Developing and operating research infrastructures and technological platforms supporting these research areas as well as original research in health physics and energy.
- Promoting the development of new technologies for science for the benefit of society and thus supporting national and European industrial competitiveness.
- Welcoming students trained at IJCLab through and for research at the heart of a world-class academic environment.

1.2 Structure

The IJCLab organization chart is shown in the figure 1.2. The laboratory's activities are structured around seven scientific poles : High-Energy Physics; Accelerator Physics; Health Physics; Energy and Environment; Nuclear Physics; Astroparticles, Astrophysics and Cosmology; Theoretical Physics. Each scientific pole is organized into teams dealing with a specific research theme. During this internship, I joined the High-Energy Physics pole in the "JLab/EIC" team of which my supervisor, Raphaël Dupré, is also assistant manager. The scientific poles are supported by an engineering pole divided into four departments (electronics, IT and computing, instrumentation and mechanical engineering). All these poles can rely on the presence of research infrastructures and technological platforms (such as ALTO, LaserIX, MOSAIC and SUPRATEch) and services (support services, administration, transverse activities).

The laboratory manager is Achille Stocchi. His directorate is constituted of an assistant manager, a general secretary, a assistant general secretary, associate directors and executive assistants. The associate directors are the heads of each scientific and engineering pole.

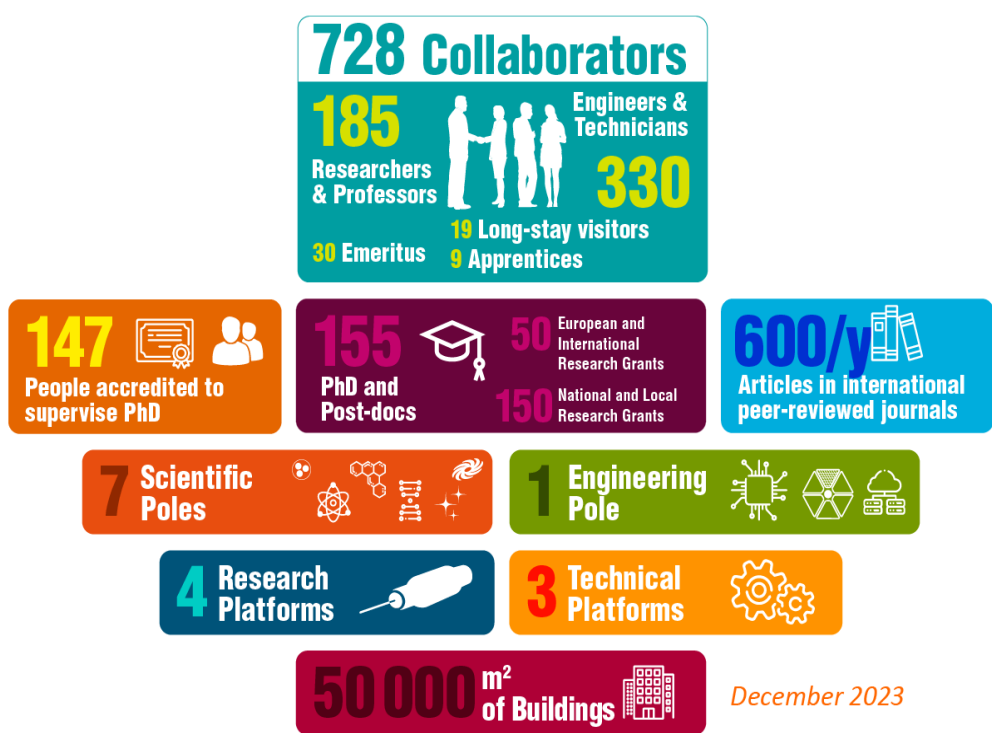


Figure 1.1: Key figures of IJCLab. Source [1].

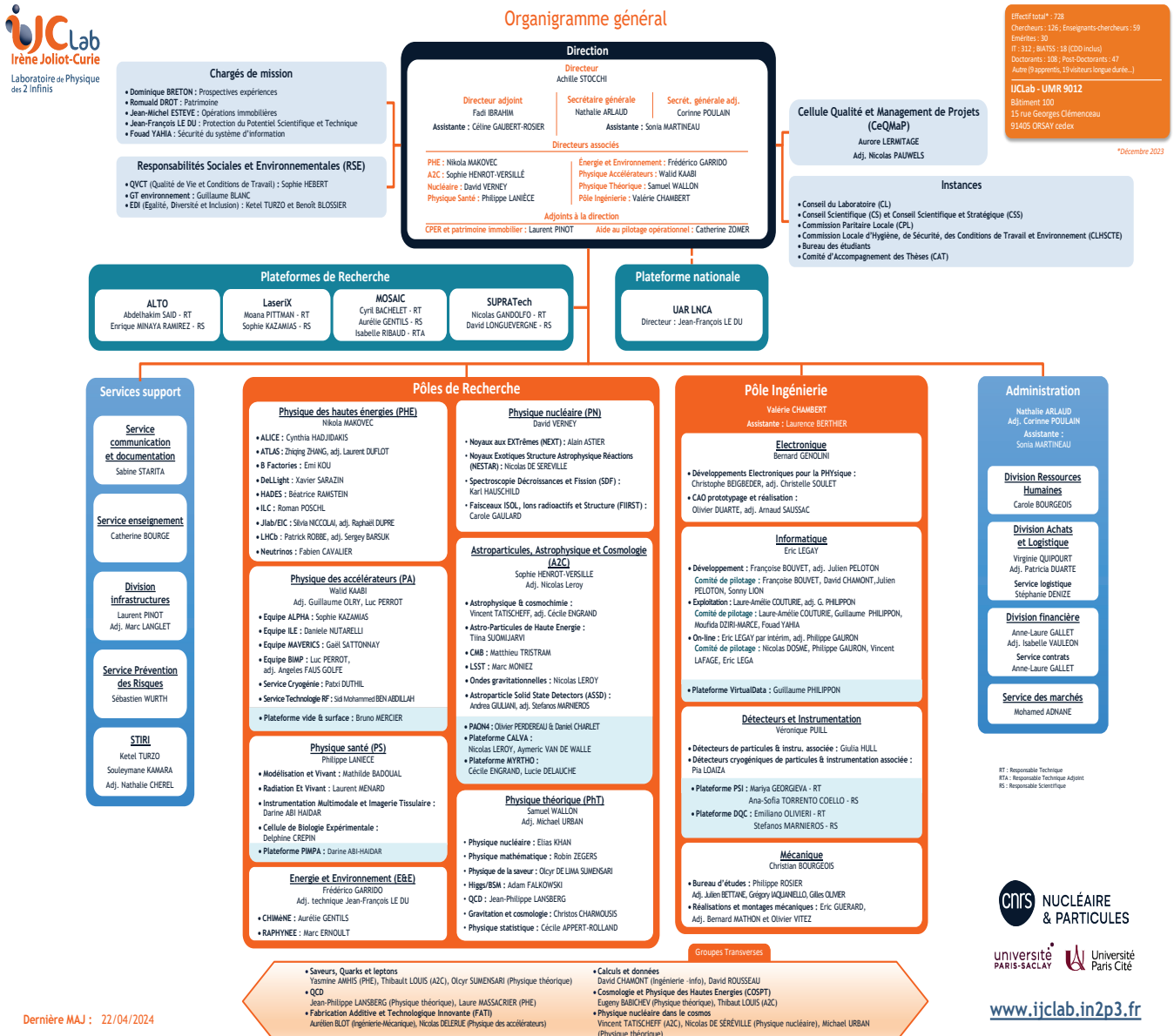


Figure 1.2: IJCLab organization chart. Source [2].

Chapter 2

Physics motivation

ALERT aims to improve the understanding of the nucleon structure through very sophisticated measurements such as the Deep Virtual Compton Scattering (DVCS) or the Tagged EMC. These measurements are motivated by either their convenience to extract nuclear Generalized Parton Distributions (GPDs) and their ability to challenge theoretical models. This chapter reviews the formalism for describing the nucleon structure. It presents the notions of structure functions in hadronic physics and an open-question associated to nuclei, the "EMC effect" named after the European Muon Collaboration.

2.1 Nucleon structure

2.1.1 Deep inelastic scattering

Considering a deep inelastic scattering of a lepton e (k) on a nucleon N (p), only the outgoing lepton e' (k') is detected and the final state of the nucleon consist of unresolved hadrons "X" (see figure 2.1).

The virtuality of the process is the quantity defined by $Q^2 = -q^2 = -(k - k')^2$. It represents the scale $\lambda = 1/\sqrt{Q^2}$ at which the incoming nucleon can be probed. The invariant mass of the final state X is given by $W^2 = (q + p)^2 \stackrel{lab}{=} M_N^2 + 2M_N\nu - Q^2$, where M_N denotes the mass of the target nucleon and $\nu = \frac{p \cdot q}{M_N} \stackrel{lab}{=} E - E'$ the transferred energy to the lepton via the virtual photon. Two conditions must be satisfied to categorize an interaction as a DIS [3] :

- $Q^2 > M_N^2 \approx 1 \text{ GeV}^2$, this allows to interact with partons instead of the whole nucleon.

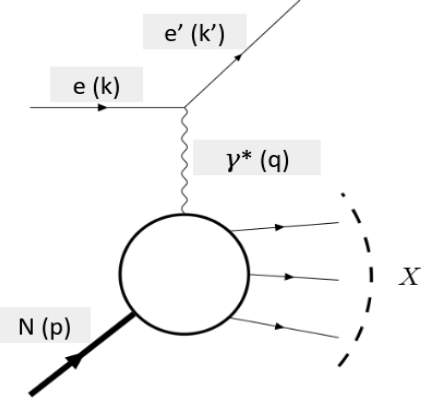


Figure 2.1: The Feynman diagram of a deep inelastic scattering at leading order. A virtual photon γ^* carries the exchanged four-momentum q . k , k' and p are respectively the four-momenta of the incoming lepton, the outgoing lepton and the target nucleon.

- $W^2 \gg M_N^2$, this allows to make sure we break down the nucleon.

The cross section of the DIS can be parameterized by two structure functions $W_1(\nu, Q^2)$ and $W_2(\nu, Q^2)$:

$$\frac{d^2\sigma}{d\Omega dE'} = \frac{\alpha^2 \cos^2\left(\frac{\theta}{2}\right)}{4E^2 \sin^4\left(\frac{\theta}{2}\right)} \left(W_2(\nu, Q^2) + 2W_1(\nu, Q^2) \tan^2\left(\frac{\theta}{2}\right) \right)$$

where α is the electromagnetic coupling constant, θ the scattered angle of the electron and $d\Omega$ the solid angle of detection. In practice, we use the structure functions $\mathcal{F}_1(x, Q^2)$ and $\mathcal{F}_2(x, Q^2)$ defined by :

- $\mathcal{F}_1(x, Q^2) = M_N W_1(\nu, Q^2);$
- $\mathcal{F}_2(x, Q^2) = \nu W_2(\nu, Q^2).$

These functions can be expressed in terms of parton distribution functions (PDFs). PDFs are mathematical functions of quark flavour q , momentum fraction x and Q^2 : $f_q(x, Q^2)$. They represent the probability of finding a quark of flavour q carrying a longitudinal momentum fraction x at a scale Q^2 . Experimentally, x can be related at leading order with the Bjorken scaling variable $x_B \equiv \frac{Q^2}{2p \cdot q} \stackrel{lab}{=} \frac{Q^2}{2M_N \nu}$. In the Bjorken limit $\{Q^2, \nu\} \rightarrow \infty$ and at a fixed x_B value, DIS can be considered as the scattering of a lepton on a free

quark. In other words, the DIS cross section on nucleon can be expressed as the sum of elastic cross section of the lepton on the different quark flavors [4] :

$$\left(\frac{d\sigma}{d\Omega dE'} \right)_{N,DIS} = \sum_q \int_0^1 dx e_q^2 f_q(x) \left(\frac{d\sigma}{d\Omega dE'} \right)_{q,ES} \delta(x - x_B)$$

where e_q is the charge of the quark q. One can determine the PDFs of the proton from fits of world data related to DIS experiments. The figure 2.2 shows the MMHT2014 global fit provided by L. A. Harland-Lang *et al* [5].

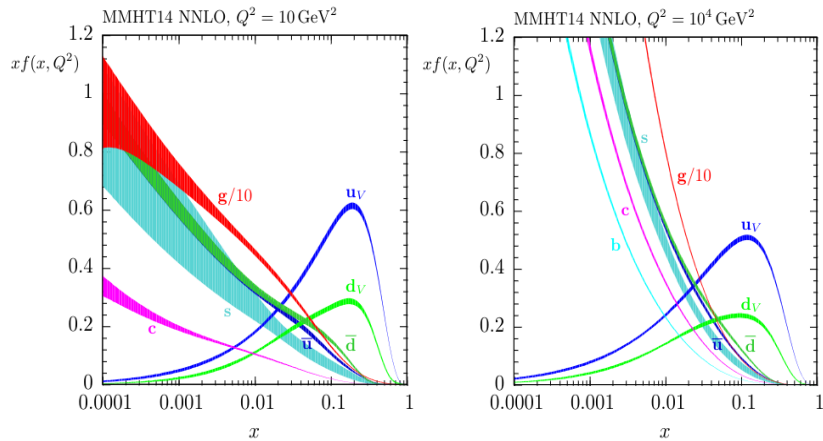


Figure 2.2: Parton distribution functions of the proton obtained by MMHT2014 Next to Next to leading order PDFs at $Q^2 = 10 \text{ GeV}^2$ and $Q^2 = 10^4 \text{ GeV}^2$, with associated 68 % confidence-level uncertainty band. Source [5].

2.1.2 Generalized parton distributions

General parton distributions (GPDs) are another set of structures functions. They are more complex and contain more information than PDFs. One can access GPDs in scatterings off nucleon where a lepton interact with a single quark without destroying the nucleon (figure 2.3). They are real structure functions $F^q(x, \xi, t)$ of variables x , ξ , Δ . These parameters are defined such that $x + \xi$ and $x - \xi$ are respectively the incoming and outgoing quark momenta and $t = \Delta^2$ is the squared transferred four-momentum [6]. These functions encode the correlation between the charge distribution of quarks in the transverse plane and the longitudinal distribution of their momenta (figure 2.4).

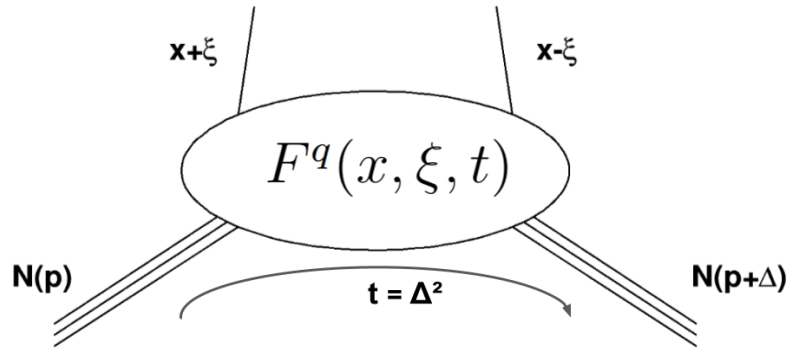


Figure 2.3: General representation of the GPDs of a nucleon represented by the triple line and noted N. Single lines represent quarks or anti-quarks probed in the nucleon. Source [6, p. 6].

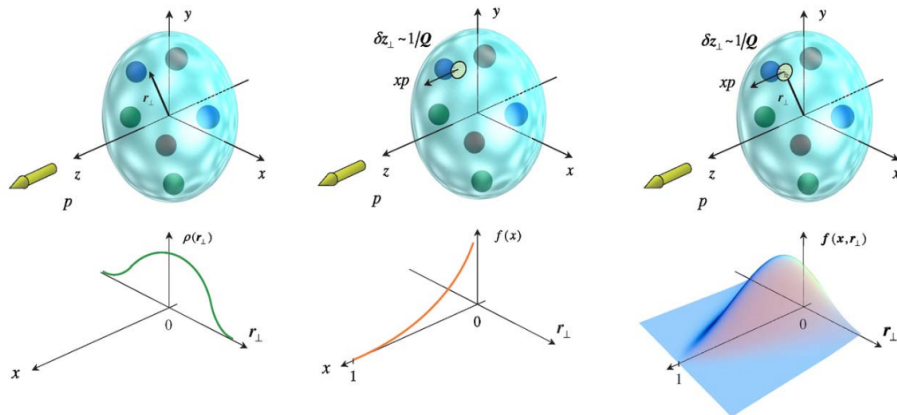


Figure 2.4: Illustration of form factors (left), parton distribution functions (center) and generalized parton distributions (right). Source [7, p. 91]

2.1.3 EMC effect

The EMC effect is a surprising phenomenon observed at the nuclear scale. It highlights the dependence of the nucleon properties on the nuclear environment. Indeed, the binding energy of nucleons inside nuclei is of the order of few MeV while the mass of nucleons is about 1 GeV. So one could expect that the parton distribution of bound nucleons inside a nucleus should be identical to the parton distribution of a collection of the same number of free nucleons. In this sense, DIS experiments which are sensitive to the partonic structure of the nucleon would give the same result for all nuclei [8]. Instead, the European Muon Collaboration (EMC) found that the per-nucleon (e, e') cross section ratio of iron to deuterium is not unity [9]. The figure 2.5 is an image of the EMC data as it appeared in the November 1982 issue CERN Courier. Since then, various theoretical models try to explain this observation. ALERT expects to provide new tests to discriminate some of these models.

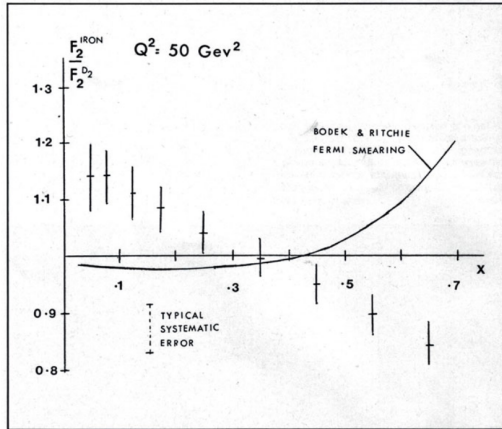


Figure 2.5: Ratio of the $\mathcal{F}_2^{IRON}(x, Q^2)$ structure function of iron over the $\mathcal{F}_2^{D2}(x, Q^2)$ of deuterium. Source [10].

2.2 Proposed measurement

The scientific program of the ALERT experiment is very wide. Among the various processes that will be measured are the DVCS and the Tagged EMC of the ${}^4\text{He}$ nucleus.

2.2.1 DVCS

The Deeply Virtual Compton Scattering (DVCS) is an exclusive process in which a single real photon is produced in the final states of an electron scattering off a nucleus (figure 2.6). DVCS processes are the simplest to access GPDs. A spin-0 nuclear target as the ${}^4\text{He}$ has only one GPD noted $H_A = H_A(x, \xi, t)$; this considerably reduces complexity compared with the proton, which has four GPDs.

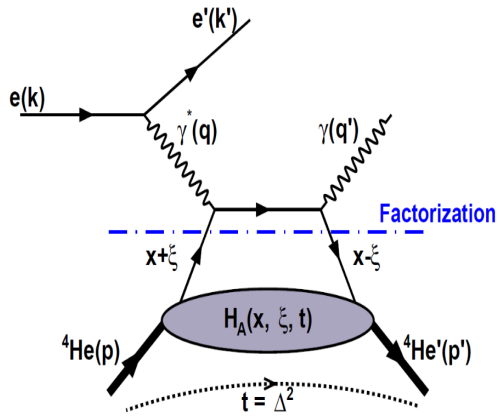


Figure 2.6: Feynman diagram of a DVCS. Source [6, p. 8].

2.2.2 Tagged EMC

The tagged EMC measurement is based on the spectator mechanism (also called plane wave impulse approximation (PWIA)). This is a process where a single virtual photon interacts with a DIS on a nucleon and the rest of the nucleus remains intact and unaffected. It is called the spectator and noted $A - 1$ (figure 2.7). DIS cross sections will be measured and studied as a function of the kinematic variables of the recoil nucleus detected by ALERT.

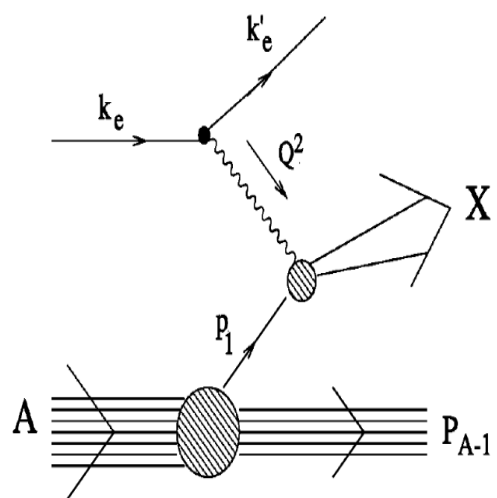


Figure 2.7: The process $A(e, e'(A - 1))X$ within the impulse approximation.
Source [11, p. 13].

Chapter 3

ALERT at Jefferson Lab

The ALERT experiment will take place in the premises of the Thomas Jefferson Accelerator Facility (Jefferson Lab or JLab). Jefferson Lab is a U.S. Department of Energy Office of Science national laboratory. It has been founded in 1984 and is located in Newport News, Virginia, USA. The JLab's research program stands on its Continuous Electron Beam Accelerator Facility (CEBAF). This chapter presents the experimental setup of the experiment with a focus on **a** (new) low energy recoil tagger, i.e ALERT.

3.1 CEBAF

The accelerator is composed of two linear accelerators (linacs) based on superconducting radio frequency technology, connected by two recirculating arcs and arranged in race-track configuration (figure 3.1). It can deliver spin polarized electrons with energies ranging up to 12 GeV. Electrons are generated in a gun and pre-accelerated in an injector before entering the first linac. The system is able to redirect the accelerated electron beam to one of the four experimental halls each time it passes through a linac. This makes it possible to work with different beam energies. Each hall is dedicated to a specific program of physics [12]. The ALERT detector will be integrated inside the spectrometer CLAS12 located in the Hall-B.

3.2 CLAS12

CLAS12 stands for **C**EBAF **L**arge **A**cceptance **S**pectrometer for operation at **12** GeV. It consists of a set of sub-detectors aligned along the beam line in the Hall-B (figure 3.2). These detectors are divided into two categories: forward and central detectors. Central detectors are immersed in a

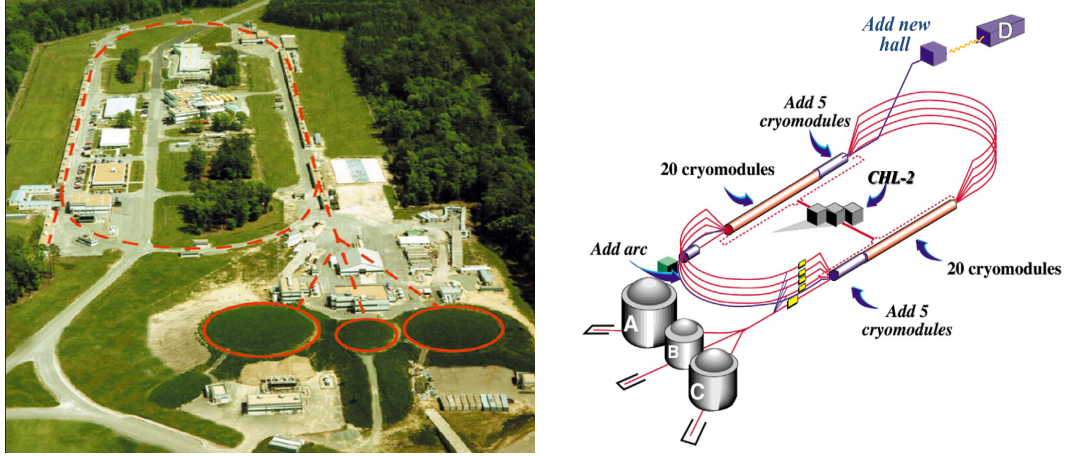


Figure 3.1: (Left) Aerial view of the Jefferson Laboratory. The CEBAF continuous electron beam accelerator is represented. The dashed lines indicates the location of the accelerator, and the circle indicates the location of three experimental halls. (Right) Schematic view of the CEBAF. The linacs are represented by the arrangement of cryomodules. The letters A,B,C,D represents the four experimental halls. Source [13, 14].

strong solenoid magnetic field of 5 T while forward detectors are placed in or just after a torus magnet [14]. They are typically drift chambers (DCs), Cherenkov counter (LTCC, HTCC), time-of-flight systems (FTOF, CTOF), electromagnetic calorimeters (ECAL), silicon vertex tracker (SVT) and barrel micromegas tracker (BMT).

The forward part of CLAS12 ensures the detection of particles with θ angle¹ ranging from 0° to 35° while the central part ensures the detection of particles with θ angle ranging from 35° to 125° .

3.3 ALERT

The ALERT detector is composed of an hyperbolic drift chamber (AHDC) and a time-of-fight (ATOF) system. The figure 3.3 shows the schematic layout of the ALERT detector. It will replace the Silicon Vertex Tracker (SVT) and the Barrel Micromegas (BMT) in the central part of CLAS12 (see figure 3.2). The table 3.1 summarizes the types, the momentum ranges and the angular distributions of the particles to be detected with ALERT during each proposed measurements.

¹Angles are given in spherical coordinates.

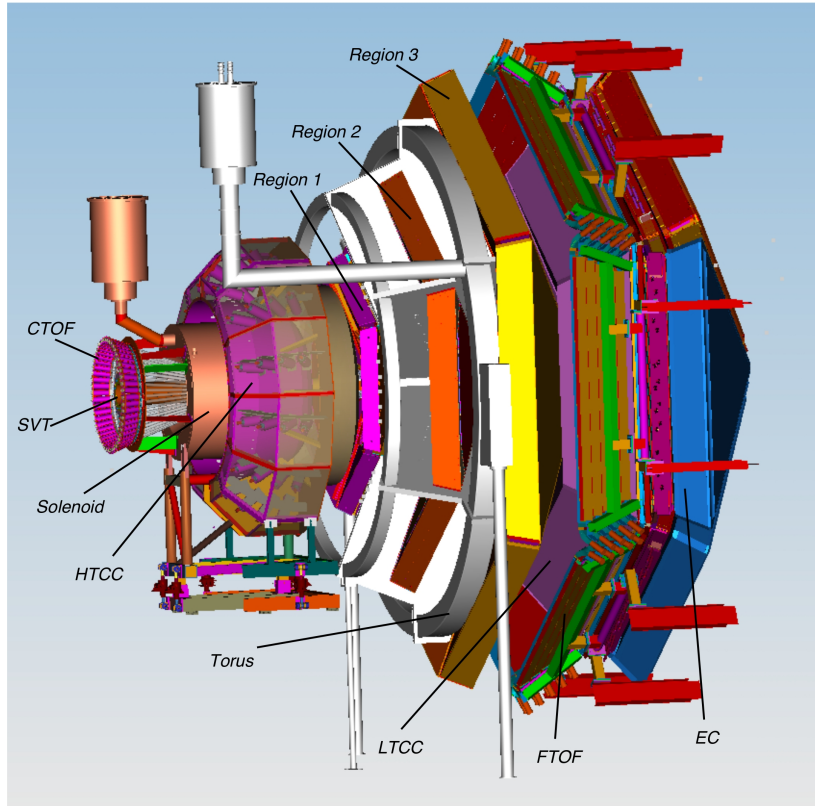


Figure 3.2: The CLAS12 spectrometer in Hall-B. The central detectors are contained in the solenoid magnet. The other detectors constituted the forward part of CLAS12. Source [15, p. 30].

Measurement	Particles detected	p range	θ range
Nuclear GPDs	^4He	$230 < p < 400 \text{ MeV}$	$\pi/4 < \theta < \pi/2 \text{ rad}$
Tageed EMC	$\text{p}, ^3\text{H}, ^3\text{He}$	As low as possible	As close to π as possible
Tagged DVCS	$\text{p}, ^3\text{H}, ^3\text{He}$	As low as possible	As close to π as possible

Table 3.1: Specific requirements for the particles to be detected by ALERT. Source [15, 11].

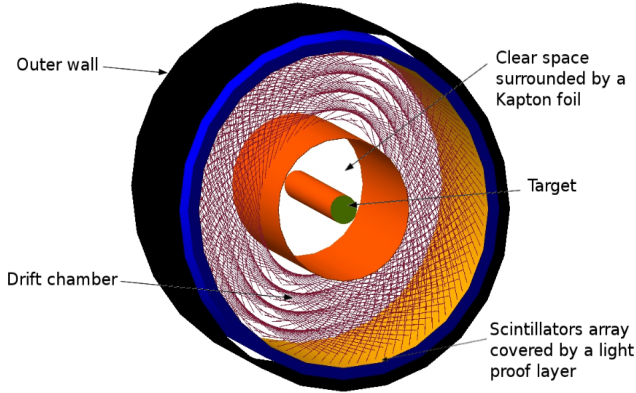


Figure 3.3: 3D view and cutting plan of the layout of the ALERT detector. Source [16, p. 50].

3.3.1 AHDC

The drift chamber of ALERT is a gaseous detector filled with a mixture of He (80 %) and CO₂ (20 %). The tracking of charged particles is ensured by a set of 3026 wires distributed over 21 circular layers centered on the beam axis [16]. The wires are alternatively oriented either in -10° or $+10^\circ$ with respect to the axis of the drift chamber to allow the determination of coordinates along the beam axis (z). The wires disposition of ALERT is shown in figure 3.4 and 3.5.

3.3.2 ATOF

The time-of-flight system will surround the AHDC. It is constituted of two layers of scintillators read by silicon photomultipliers (SiPM). The study of the time-of-flight combined with the AHDC track will allow the identification of particles by ALERT : this is the reconstruction (appendix A.2).

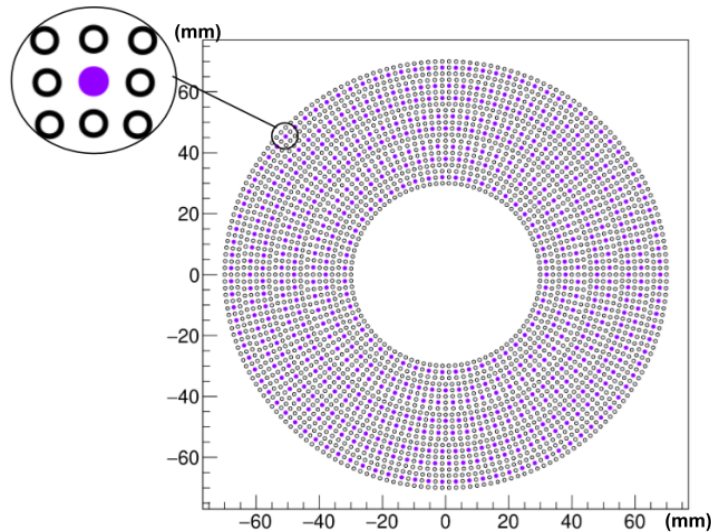


Figure 3.4: Wires disposition of the drift chamber of ALERT. A detection cell is highlighted. It is composed a sense wire ● surrounded by eight field wires ○. A potential difference is established between the sense (+) and the field (−) wires to ensure the drift of the electrons created by ionization after the passage of a charged particle. It remains to process the signal collected by the sense wire to determine the position of the particle (see chapter 4).

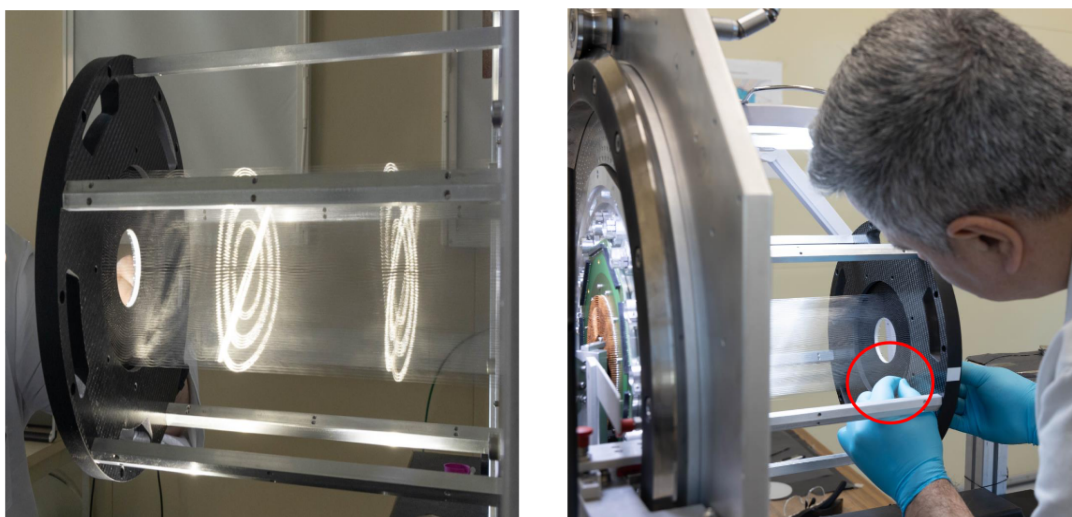


Figure 3.5: Picture of the drift chamber of ALERT taken on the premises of IJCLab. On the left, the light of two cell phones is reflected by the sense wires of each super-layers. The 20° (from -10° to $+10^\circ$) stereo angles between the wires is clearly visible.

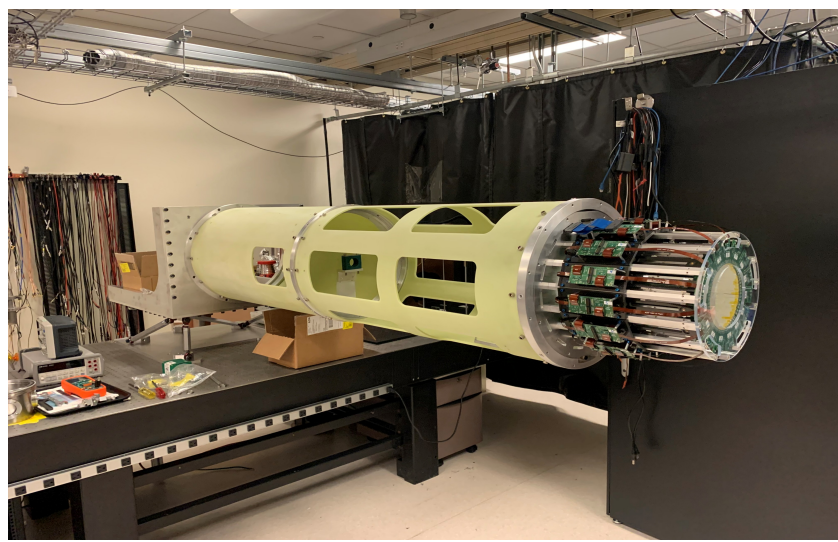


Figure 3.6: Picture of the time-of-flight system of ALERT taken on the premises of ANL. The ATOF is fixed at a cart tube.

Chapter 4

ALERT Simulation

The simulation of the behaviour of ALERT during an experiment aims to provides useful data for the development of reconstruction algorithms. The reconstruction is the part of the instrumental chain that uses the tracking data from AHDC and time-of-flight data from ATOF to make the particle identification. The full-knowledge of the system in simulation make it possible to quantify the efficiency and the robustness of our algorithms. This chapter focus on the simulation of the AHDC signal.

4.1 Presentation

When a charged particle passes through the volume of the drift chamber of ALERT, it ionizes the molecules of the gas and creates primary electrons. The electromagnetic field generated by the potential difference between the sense and field wires ensures the drift of these electrons towards the closest sense wire. Without the presence of a magnetic field, it can be show that the electric field is radial and inversely proportional to distance to the sense wire. In presence of an external magnetic field such as the 5 T of the solenoid magnet of CLAS12, the field lines take a more complex form as show in figure 4.1. In any case, the primary electrons get more and more energy during the drift; their energies become high enough to ionize new molecules of the gas and create secondary electrons. The process {drift, get more energy, ionize} is repeated from the secondary electrons, and so on. That leads to an electronic avalanche. This is the accumulation of charges on the sense wire that generates the signal of the AHDC (figure 4.2). During the development of the drift chamber, on-beam measurements at ALTO¹ has been done. The

¹ALTO is a research platform located in Orsay, France.

typical signal of ALERT is given by the figure 4.3. The following sections describe the process used to retrieved this kind of signal in simulation.

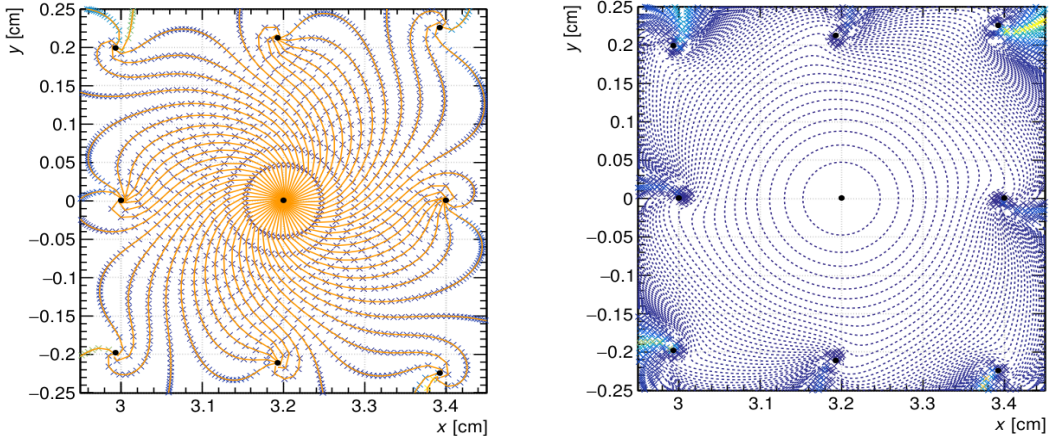


Figure 4.1: (Left) Drift trajectory of electrons in ALERT for a potential difference of 1.5 kV between the wires in a 5 T magnetic field. The sense wire is at the center and is surrounded by eight field wires. Each cross **x** is 5 ns apart. (Right) The corresponding isochronous map. Two electrons generated on the same isochronous (closed curve) will reach the sense wire at the same time. Source [16, p. 64].

4.2 Digitization

The simulation of the ALERT detector is done using GEMC². GEMC is a C++ framework that used Geant4 to simulate the passage of particles through matter. In a very simple manner, one can generate particle of any kind using GEMC. The user only have to specify the initial position and momentum of the particle in a configuration file called `alert.gcard`. The figure 4.4 shows the momentum distribution of protons generated over ten thousands events.

4.2.1 Event in GEMC

Let consider the propagation of a proton during one event. In GEMC, the track of this particle is segmented in "steps". To simplify, a "step" can be considered as one of the multiple points calculated by Geant4 with the particularity to be a C++ object that contains informations such as :

²GEMC : GEant4 Monte-Carlo

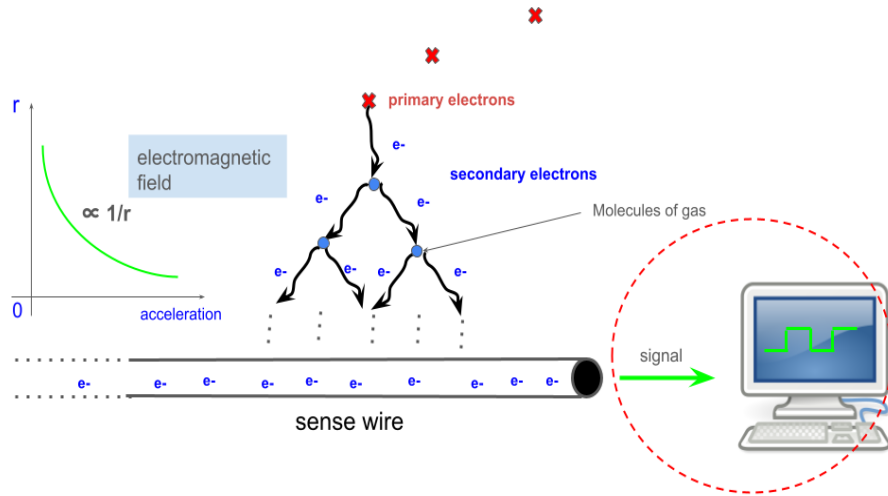


Figure 4.2: Mechanism that leads to the signal measured by the drift chamber of ALERT.

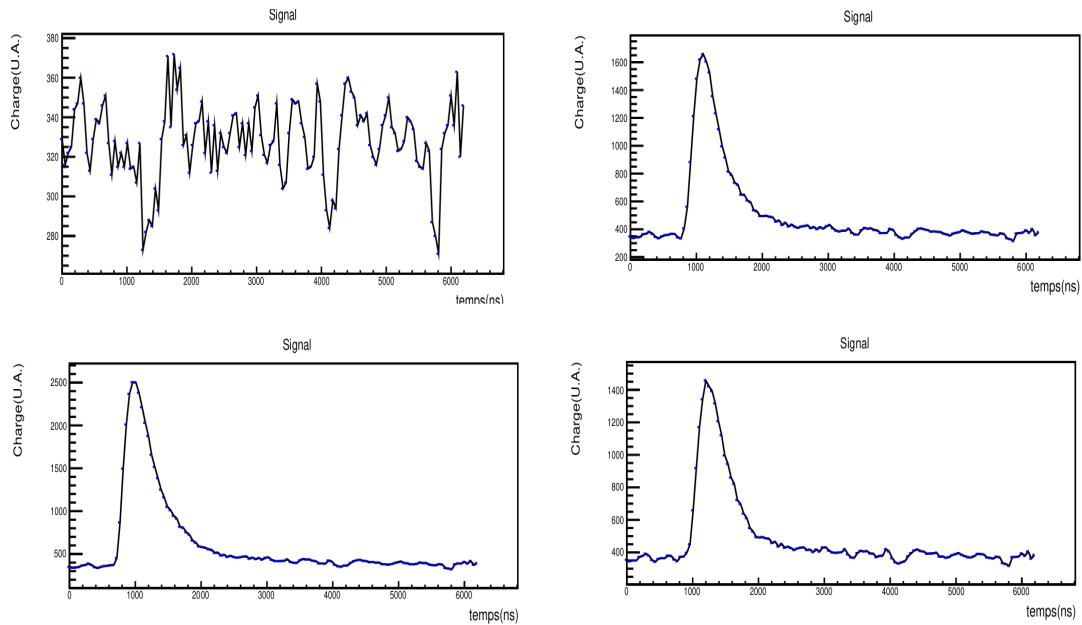


Figure 4.3: Signal measured on beam at ALTO by four sense wires during the passage of an α particle of 344 MeV/c. In the first one, no particle passed in AHDC, so the electronics only measured the noise. In the last three, a signal characteristic of an electronic avalanche has been measured due to the passage of a particle in the sensing area. Source [16, p. 94].

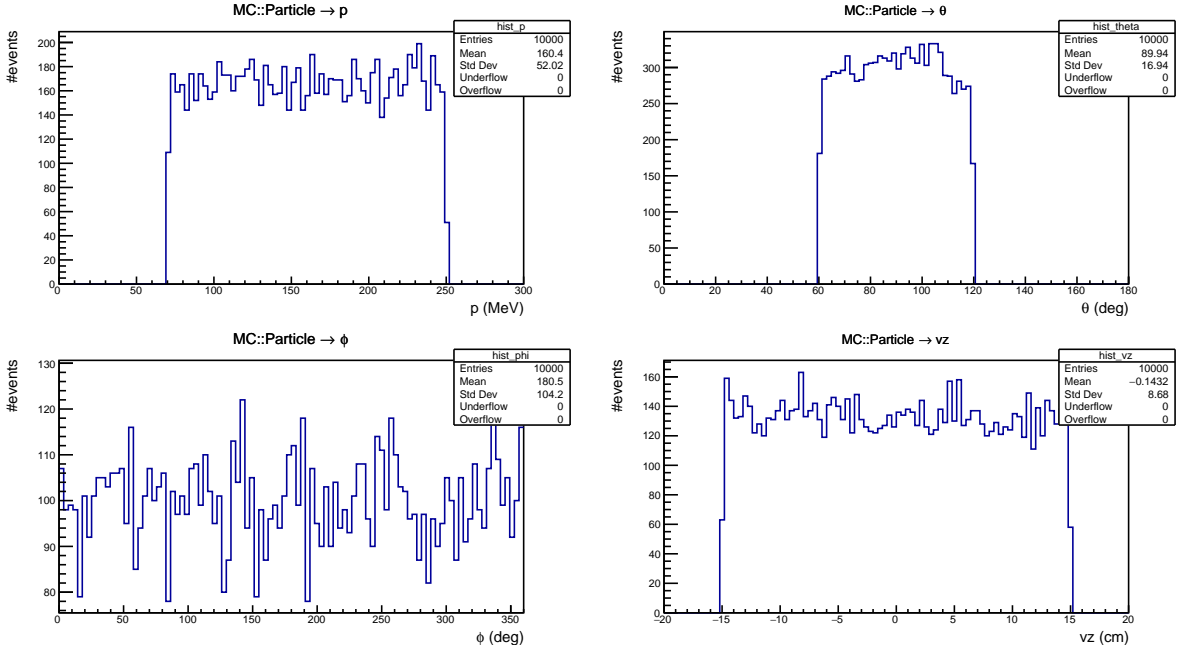


Figure 4.4: Momentum distribution of initial protons generated over ten thousands events in **GEMC**.

- the energy deposited in the medium between the previous step and the current step (ΔE);
- the local and global coordinates of the step/point (x, y, z);
- the momentum of the particle at this step of the process (p_x, p_y, p_z);
- the identifiers of the detector volume where it has been calculated;
- and so on...

A cell detection of ALERT is encoded by a 3D volume as shown in figure 4.5. Choosing a sense wire to study corresponds dealing with all the steps calculated (or appearing) in the sensitive zone associated to this sense wire. In **GEMC**, these steps are encoded in a C++ object called **MHit**. The figure 4.6 shows the distributions of deposited energy, Geant4 time, r position and z position that we can find in a particular **MHit** object.

4.2.2 Drift time calculation

The section 4.1 explains the process that leads to the detection of a signal in a given AHDC wire. One characteristic of great importance is the drift time.

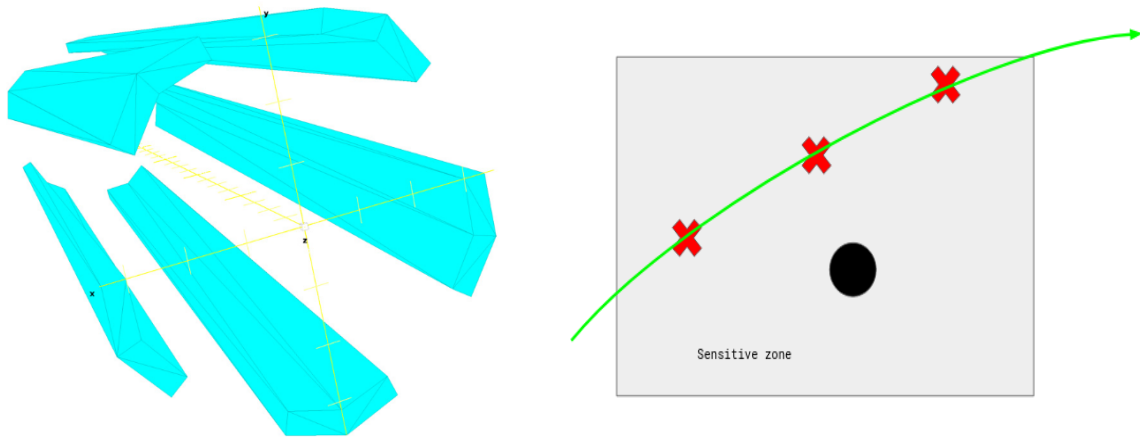


Figure 4.5: (Left) AHDC-like cells with exaggerated concavity for easier visualisation. (Right) A set of steps (**x**) calculated in the same detection cell. The green line represents the trajectory of a particle.

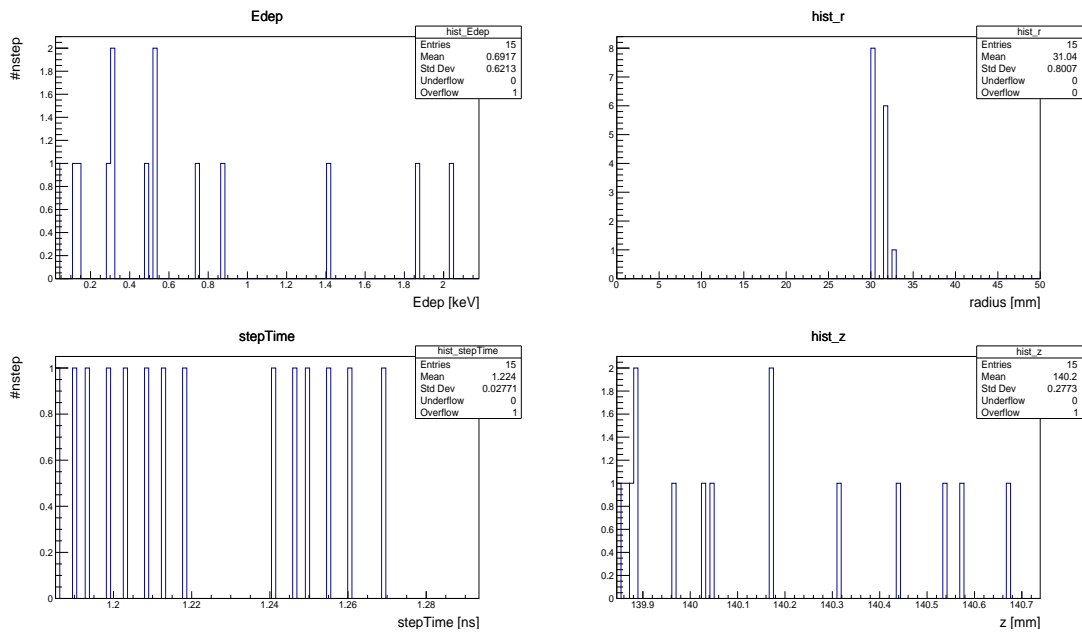


Figure 4.6: Distribution of energy deposited, geant4 time, r position and z position of a particular **MHit** object. This **MHit** contains 15 steps.

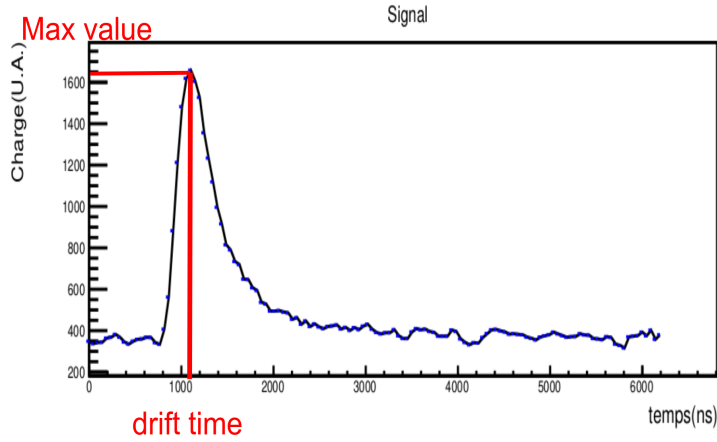


Figure 4.7: Display of the drift time associated with the signal

Looking at a typical signal measured on beam (figure 4.3), one can assume that the maximum of the distribution is reached when the "first" primary electron that has been created by ionization finally reaches the sense wire: we assume this moment to be the drift time (4.7).

It is important to note that we don't have access the drift time in GEMC. Fortunately, we have can benefit of the work done by Lucien CAUSSE [16] during the development of ALERT. Indeed, the isochronous map of the figure 4.1 shows a relationship between the place where the primary electron has been created and the moment it reaches the sense wire (i.e the drift time). The figure 4.8 shows the mapping, made by Lucien, that expresses the drift time t_d as a function of the distance D : $t_d = f(D)$. This distance corresponds to the distance of closest approach, also called *docta*. It is defined as the distance from a "step" point to the sense wire and perpendicular to the wire. With the notations of the figure 4.9, it be can expressed as³:

$$D = H_{abh} = L_{ah} \sqrt{1 - \left(\frac{L_{ah}^2 + L_{ab}^2 - L_{bh}^2}{2 \cdot L_{ah} \cdot L_{ab}} \right)^2} \quad (4.1)$$

All distances $L_{ab,ah,bh}$ are accessible in GEMC. Finally, the process to compute determine the drift time is the following :

0. (reminder : a drift time can be associated to each "step"/"point")
1. compute the docta using the formula 4.1;

³Short demonstration in A.1

2. add a resolution effect using the relation $\sigma_{ech} = f(D)$ of the figure 4.8; D becomes a draw of the normal distribution $\mathcal{N}(D, \sigma_{ech})$;
3. use the relation $t_d = f(D)$ of the figure 4.8 to compute the drift time.

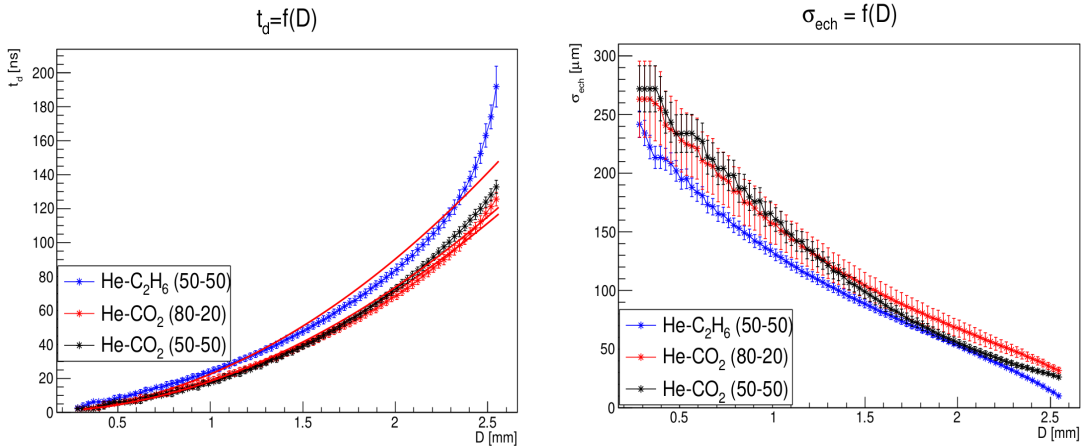


Figure 4.8: (Left) Drift time of primary electrons as a function their initial distance to the wire for various gaseous mixtures. The potential difference is still 1.5 kV, the drift chamber being in a 5 T magnetic field. (Right) Estimation of the spatial resolution of the detector as a function of the distance to the step. Source [16].

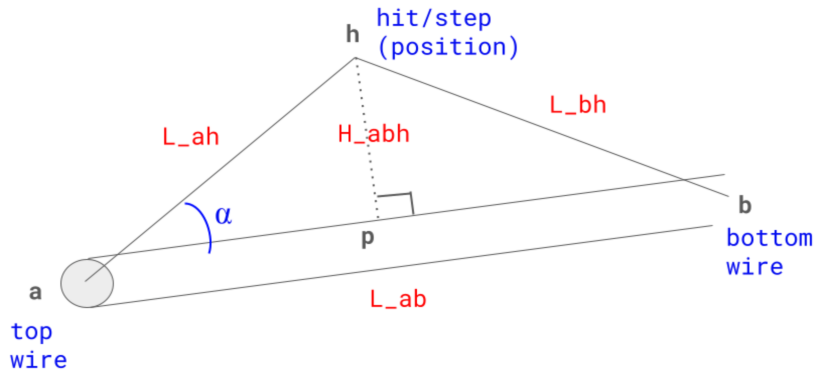


Figure 4.9: Distance of closest approach (doca). H_{abh} is the doca.

4.2.3 Signal generation

We use an empirical approach to generate the AHDC signal. Indeed, removing the noise, we have first looked at well-known probability density distributions which could have a shape similar to the one of the figure 4.7. We have selected the Landau distribution. The Landau distribution depends on two parameters μ and c : $\mathcal{L}(t; \mu, c)$. μ is the location parameter, the place where the distribution reaches its maximum (the most probable value). c is the scale parameter; for example, it controls the width at mid-height (without being it !). The process to generate the signal is the following.

Stage 1

Using the results of section 4.2.2, we can plot the energy deposited in each "step" as a function of the associated drift time. The figure 4.10 shows the mass distribution obtained in one AHDC wire.

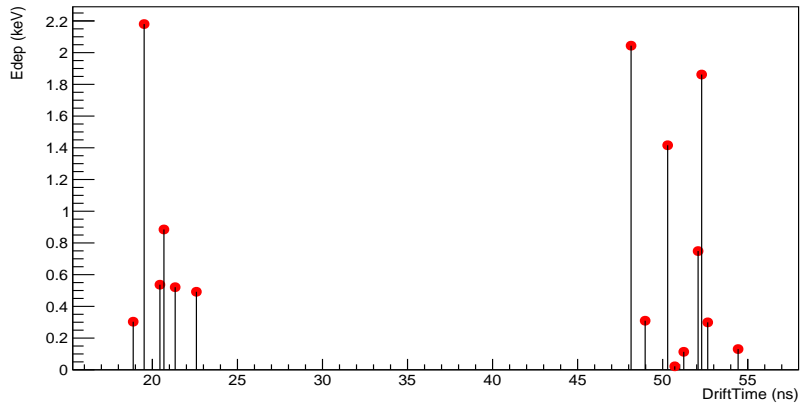


Figure 4.10: The energy deposited in each steps as a function of the drift time.

Stage 2

We replace each mass with a distribution spread over time. We use Landau distributions of same scale parameters $c = 240$. This value has been determined by trial and error to fit the on-beam measurements of the figure 4.3. The location of each Landau distribution is the corresponding drift time. As the signal must be a picture of the energy deposited in the sensitive zone of a AHDC wire, each Landau distribution is weighted by the corresponding deposited energy. Finally, we add a delay of 1000 ns. Before summing

all distributions, we obtain the result of the figure 4.11. After summing all distributions, we obtain the result of the figure 4.12.

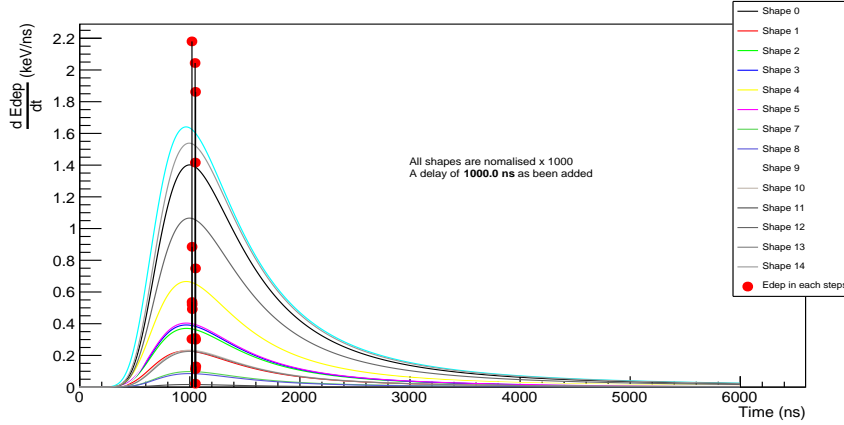


Figure 4.11: Simulation of the AHDC signal : before summing all Landau distributions. The distributions have been multiplied by 1000 for a better view. The time window, the delay and the scale parameter of the Landau distributions as been chosen to fit the result of the figure 4.3.

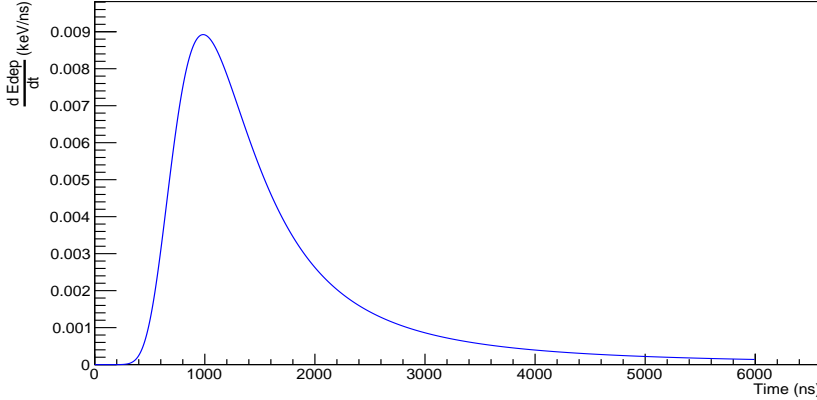


Figure 4.12: Simulation of the AHDC signal : after summing all Landau distributions.

Stage 3

The ALERT detector doesn't measure signal in keV/ns. Instead, its electronics will provide a signal in a certain unit called ADC. To go from keV

to ADC, we use a proportionality factor called *electron yield*. To anticipate the digital processing of the signal, we sample it every 44 ns. To simulate electronic noise, we add to each sample a draw from the normal distribution $\mathcal{N}(300, 30)$. The figure 4.13 shows a simulation of the electronics noise and the figure 4.14 shows a the simulation of AHDC signal.

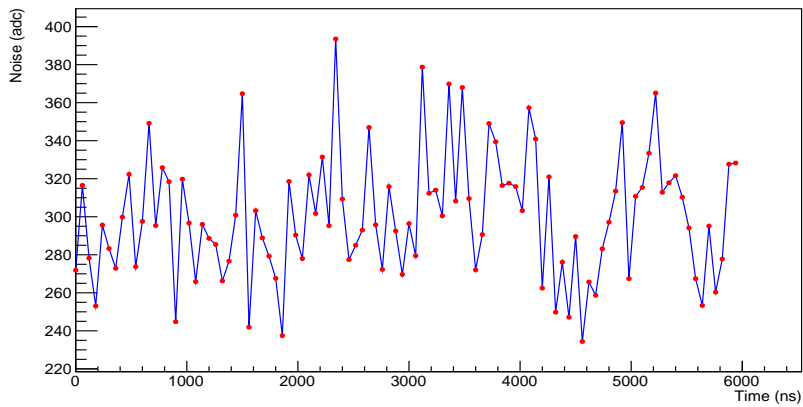


Figure 4.13: Simulation of the electronics noise. Each point represents a sample, a draw of $\mathcal{N}(300, 30)$.

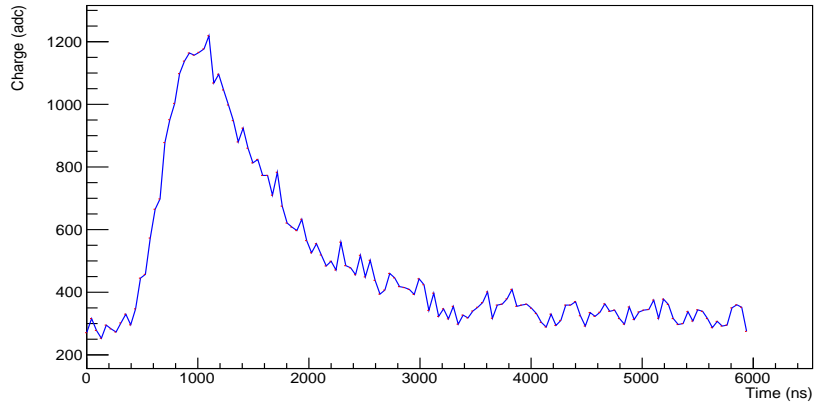


Figure 4.14: Simulation of the AHDC signal : final result. This figure must be compare to the on-beam measurement of the figure 4.3.

Results

The signal obtained in figure 4.14 has the same appearance that one we could measure in a real experiment. The goal was not to obtain the exact image of figure 4.3 but to implement a framework that can generate a realistic and an exploitable signal for further development of the ALERT software. A diagram of the framework is given by the figure 4.15. Here is a description of each setting parameter.

- **samplingTime** : defined at 44 ns, is used for the sampling of the signal;
- **adc_max** : is the maximum integer that can be written with 12 bits, i.e $2^{12} - 1 = 4095$
- **electronYields** : has been defined at 10^5 for the conversion of keV/ns to ADC (from fig. 4.12 to fig. 4.14); this parameter will play a great when comparing the signals generated by two different particles. As the particles α are expected to be more energetic than the protons, one could imagine that this value of the **electronYields** is to high because it will easily saturate the signal. On the other hand, a smaller value may reduce the amplitude of the signal generated by protons and therefore prevent their detection. Choosing the best value can only be done statistically, using real data;
- **delay** : is the delay that has been added in the stage 2 of the signal generation;
- **tmin** and **tmax** : set the time window for plots.

4.3 Decoding

The framework developed in the section 4.2.3 can provide us with a large number of exploitable and realistic signals to test reconstruction algorithms. The decoding is the stage of the instrumental chain that precedes the reconstruction. Its role is to extract relevant information from AHDC signals. The figure 4.16 shows the kind of information we can extract from the signal of the figure 4.14.

- **max_value** is the amplitude of the signal. It is important to note that at this stage we only have a digitized signal. A way to extract a precise value of this amplitude is to do a Gaussian fit using 5 or more

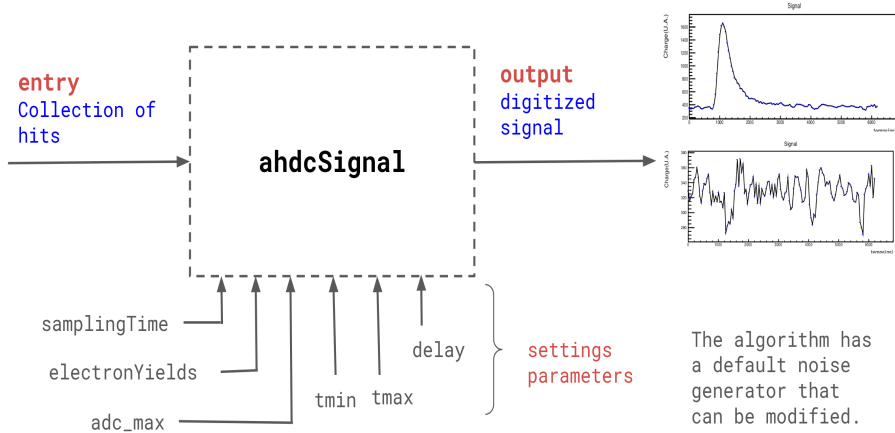


Figure 4.15: Diagram of the framework used to simulate the AHDC signal. One can play with all the mentioned setting parameters to improve the results of the simulation but also with the scale parameter of the Landau distribution.

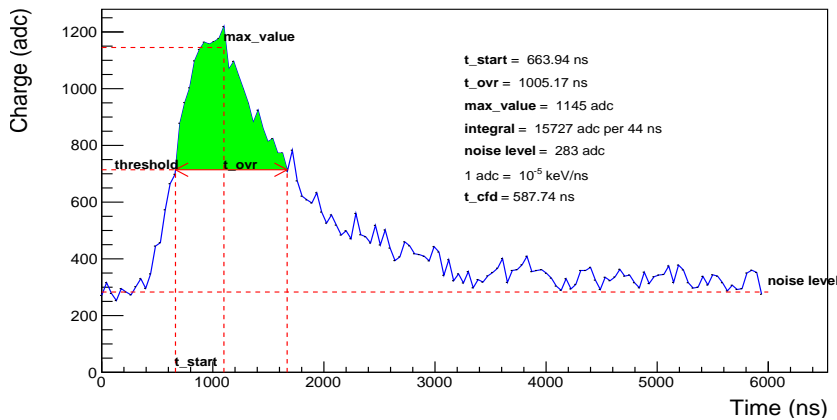


Figure 4.16: Decoding of the AHDC signal of the figure 4.14.

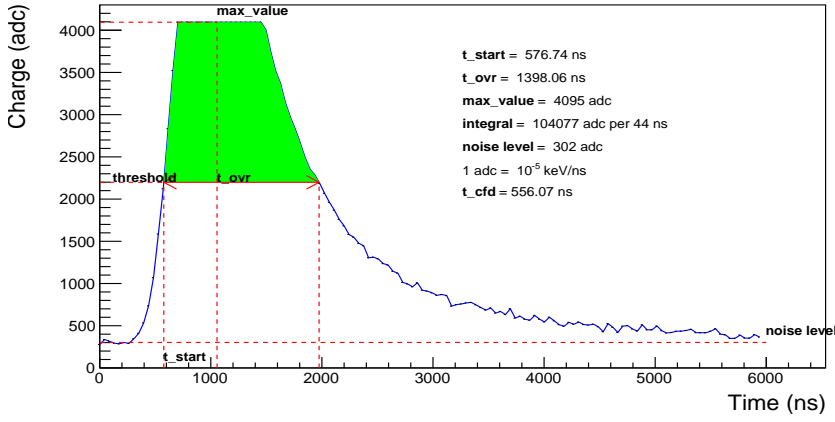


Figure 4.17: Example of a saturated signal.

points around the sample maximum and theoretically determine the maximum of this Gaussian. However, this decoding algorithm needs to be very fast, whereas fits usually take a long time. We have do it simple : the amplitude is simply the average of the 5 samples around the sample maximum. Actually, it may appears that the signal is saturated like in the figure 4.17. In that case, the amplitude corresponds to the `adc_max` but the moment when the signal reach it is the middle of the plateau.

- **noise_level** also called pedestal gives an indication the mean value of the noise. As we can't predict the noise, for the moment, we're using an average of the first five samples.
- **threshold** is the half of the amplitude after removing the noise level. It is used to determine `t_start` and `t_ovr`
- **`t_start`** is the moment when the signal reaches the half of its amplitude. Because of the fluctuation due to the noise, we agree that it corresponds to the last past below the threshold and before `max_value`. As the time is also sampled, we cannot expect `t_start` having the form `t_min + i*samplingTime`. Instead, it exists i such as $t_i < t_{start} < t_{i+1}$. If S_i is the value of the signal at t_i , approximating the signal by a straight line gives the equation :

$$y = \frac{S_{i+1} - S_i}{t_{i+1} - t_i}(t - t_i) + S_i := \text{slope} * (t - t_i) + S_i$$

When $y = \text{threshold}$, $t = t_{\text{start}}$. Hence :

$$t_{\text{start}} = t_i + \frac{\text{threshold} - S_i}{\text{slope}}$$

- **t_ovr** is the time minus **t_start** when the signal falls below the threshold after having reached its maximum value. Because of the fluctuation due to the noise, we agree that it corresponds to the first pass below the threshold and after **max_value**. It is determined in the same way that **t_start**.
- **integral** is the green area shown in the figure 4.16. It is equals to the sum of all bins (samples) between **t_start** and **t_ovr**.
- **t_cfd** is the time obtained using the Constant Fraction Discriminator (CFD) algorithm. The CFD has the particularity of giving the time when the signal reaches a constant fraction of its amplitude. The process to determine this time is illustrated by the figure 4.18. The CFD depends on two parameters : a fraction factor and a delay. Currently, the fraction factor is set to 0.3 and the delay to 5 (in index units) but they have to be optimized ! The reason is given in the section 4.4.

The methods used to extract the decoding outputs currently resist to very exotics case (figure 4.20) but they can be improved. At this stage, we still need to study the relevance of these results to what we're really after: extracting the actual energy deposited and the actual drift time. This is the object of the next section.

4.4 Analysis

In this section, we statistically evaluate the quality of the decoding algorithms. To do this we look at the time. Indeed, the drift time can be considered as the moment when the particle is detected by a sense wire. We have computed this quantity in the section 4.2.2. We define the real time measured by a sense wire to be the weighted average of the drift time associated with each of its steps. The weighting factors are the deposited energy :

$$\text{mctime} = \frac{1}{\sum_s \text{Edep}[s]} \sum_{s : \text{steps}} \text{Edep}[s] * \text{DriftTime}[s]$$

This real time is noted **mctime** and have to be compared with the times extracted from the decoding, that is to say **t_start** and **t_cfd**. For this

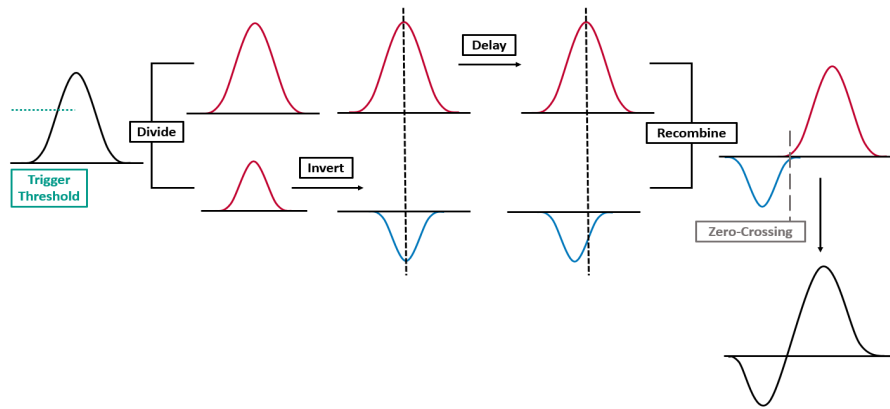


Figure 4.18: Process to extract the time using the Constant Fraction Discriminator. Source [17].

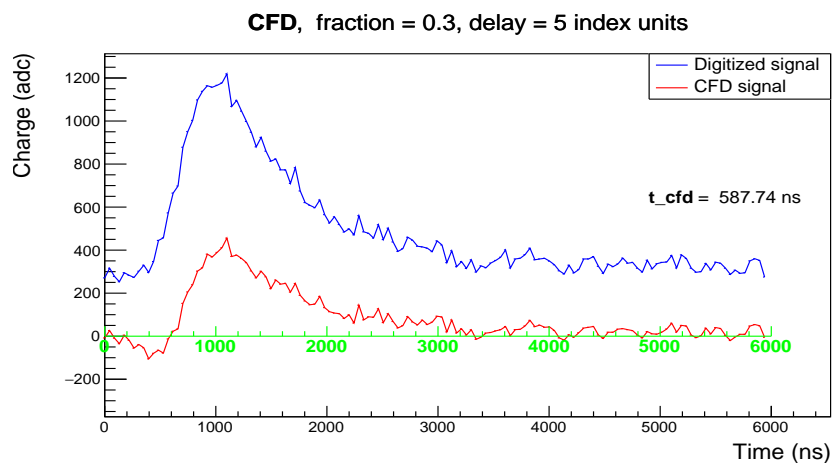


Figure 4.19: Application of the CFD on the signal of the figure 4.16.

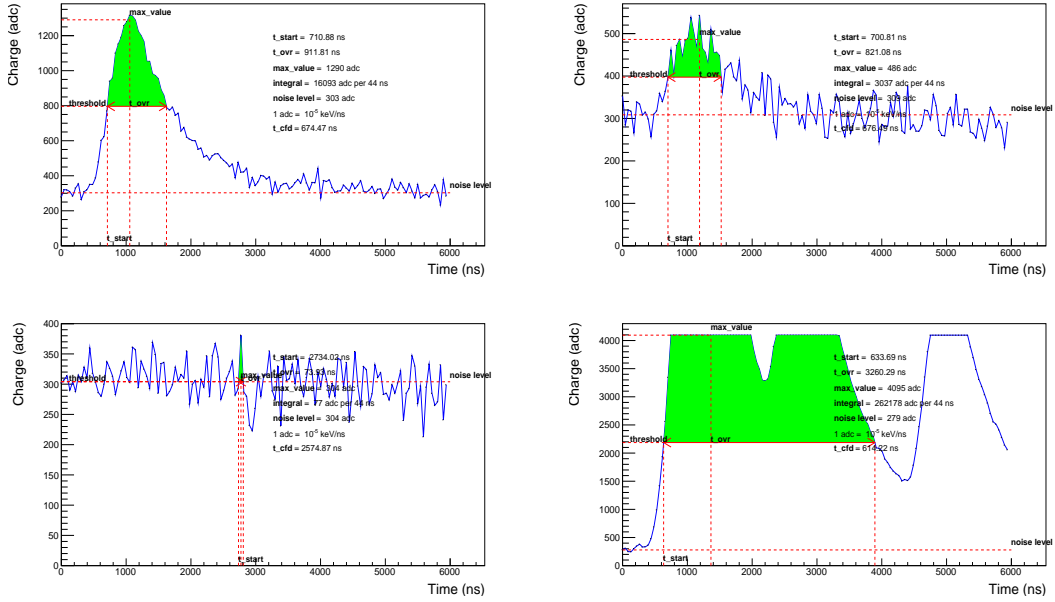


Figure 4.20: Very exotic signals. The last one is a very rare case that contributes to distorting the calculations.

purpose, we have simulated one hundred thousands events. As explained in the section 4.2.1, one event is characterized by a track that is segmented in "steps" and these steps are grouped according to whether or not they belong to the sensitive area of a "sense wire". For each wire, we save the relevant information in a HIPO⁴ file. The figure 4.21 shows informations recorded during one event. As displayed, each column represents an activated (sense) wire and each row represents a recorded data⁵. The figure 4.22 shows the histograms of all the decoding outputs.

We can already see that t_start (fig 4.22.a) and t_cf (fig 4.22.b) have the same shape. Actually, these times represent a moment when the signal reaches a "constant" fraction of its amplitude ($1/2$ for t_start and $1/3$ for t_cf in the current algorithms) but are implemented in two different ways (using the CFD or not). The figure 4.23 shows the correlations between t_start , t_cf and $mctime$. At this stage, we can only say that the three quantities are more or less related to each other. For greater precision, we

⁴HIPO stands for High Performance Output, it is a file format used in particle physics. It can be compared with the ROOT format developed in CERN.

⁵Sector, layer and component are unique. That makes it possible to identify each of 3026 wires of ALERT.

```

Choose (n=next,p=previous, q=quit, h=help), Type Bank Name or id : AHDC::adc
position for [AHDC::adc] == 62
* NODE * group = 22400, item = 11, type = 11, size =      280
    sector :          0          0          0          0          0          0          0          0
    layer :         10         11         21         30         30         31         40         40
    component :       9          9          4          14          15          15          7          6
    order :          0          0          0          0          0          0          0          0
    ADC :        508        2105        534        318        368        513        304        1571
    time :  969,4762 1015,0645 879,9039 75,3986 802,8782 864,4041 75,2402 948,1410
    ped :        289        299        313        288        285        309        306        308
    integral :      4092      33039      3566       93      1680      3430       57     21908
    timestamp :   610,7217   655,6965   781,2769 3879,7427   776,6421   697,2767 5459,9087 677,9351
    t_cfd :  579,9954 617,6946 744,9628 4569,2954 842,9095 693,3727 2738,1421 634,9743
    mctime :   34,8389   50,0197   169,2764  88,9773 128,9019  84,5588 184,0005  67,2197
    nsteps :          2         10         1         2         1         2         1         11

```

Figure 4.21: Structure of a HIPO file.

have computed the differences (fig 4.22.c and 4.22.d)

$$\Delta t_{start,cf} = t_{start,cf} - mctime.$$

We see that these distributions are very sharp and not centered in 0. We can note that these gaps are arbitrary because we can always translate the decoding times (for example by playing with the parameter `delay` of the framework). What really care here is the width of these distributions. The smaller the width, the better the decoding. It is here we see the interest of `t_cfd`. Indeed, its dependence on certain parameters allow us to realise an optimization study. Unfortunately, this study only make sense on real data. In simulation, we can only set up the procedure.

Another interesting study is the evaluation the decoding quality as a function of the amplitude of the signal. The result is given in the figure 4.24. The plots 4.24.a and 4.24.b are the correlations between $\Delta t_{start,cf}$ and the amplitude. We can see that the lower the amplitude, the worse the decoding, and the higher the amplitude, the better the decoding. Another way to see that is to histogram $\Delta t_{start,cf}$ for each amplitude bins (fig 4.24.c and 4.24.d) and plot the standard deviation of these histograms as a function the amplitude (fig 4.24.e and 4.24.f).

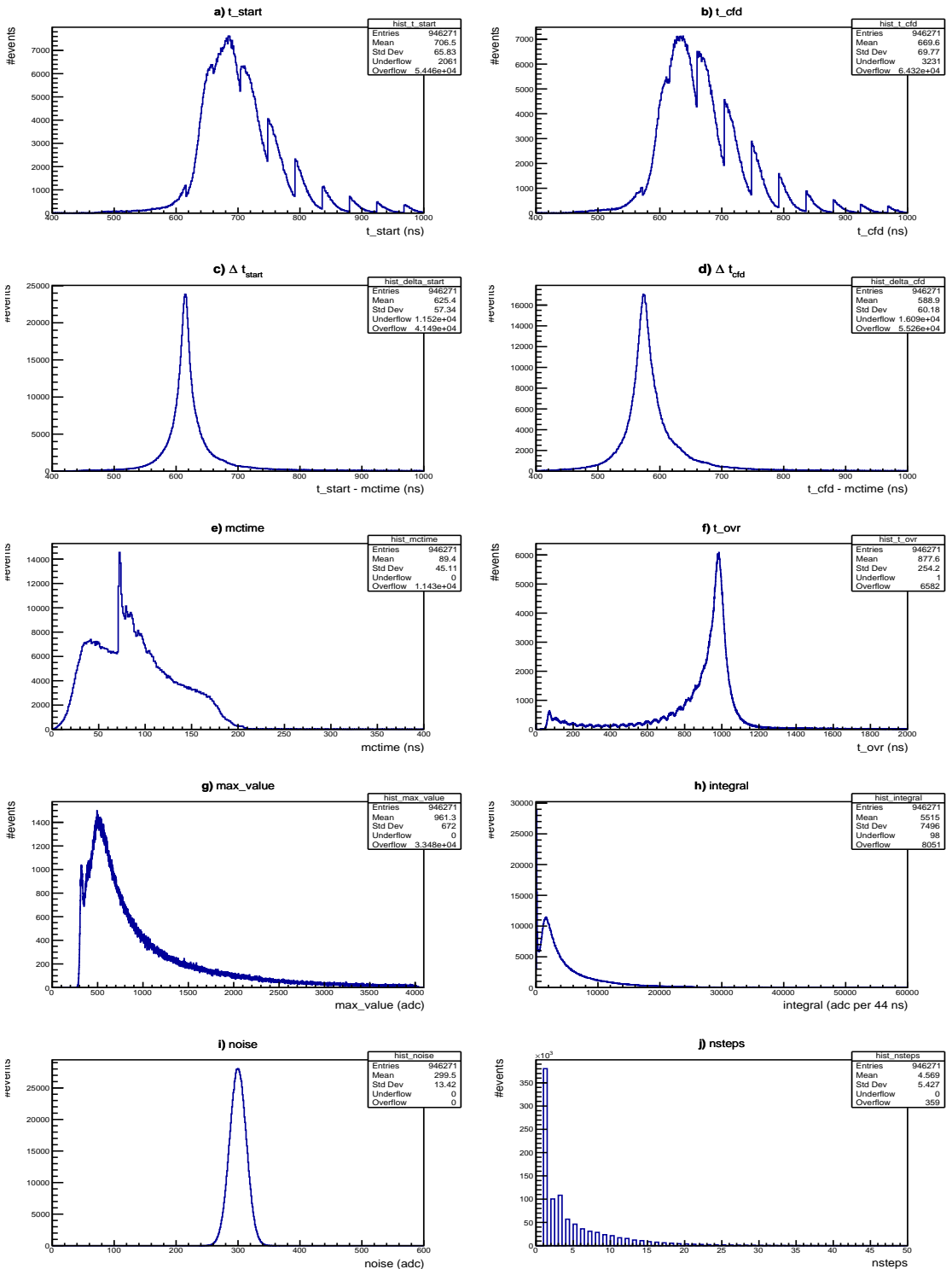


Figure 4.22: Histograms of the decoding outputs.

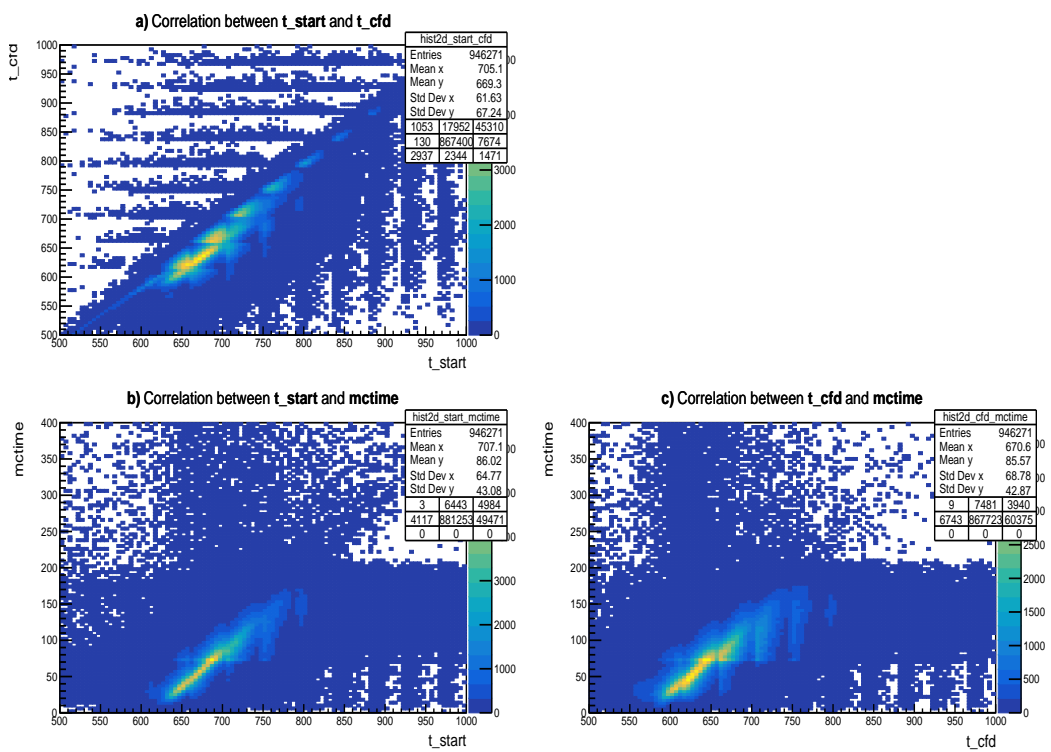


Figure 4.23: Correlation between t_start, t_cfd and mctime.

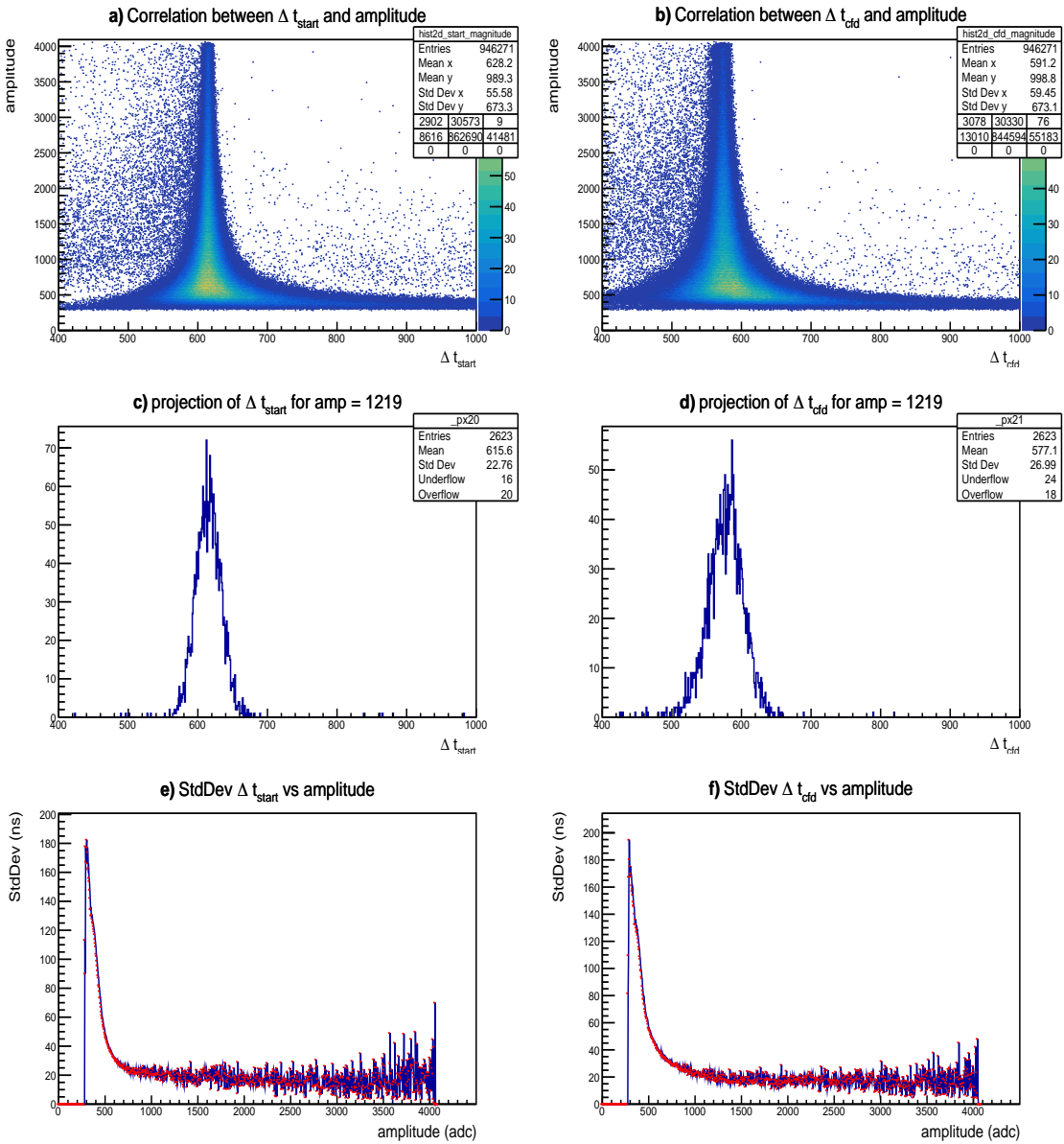


Figure 4.24: Correlations between the amplitude and the decoding quality.

Conclusion

The ALERT experiment opens up new ways for the study of nucleon structure. It is based on the development of a brand-new detector specially designed to enable measurements as sophisticated as the Deep Virtual Compton Scattering and the Tagged EMC. As with any modern detector project, an important part of the development of ALERT is dedicated to its software. In order to write efficient and robust algorithms, it was necessary to perfectly simulate the response of the ALERT detector during on-beam measurement.

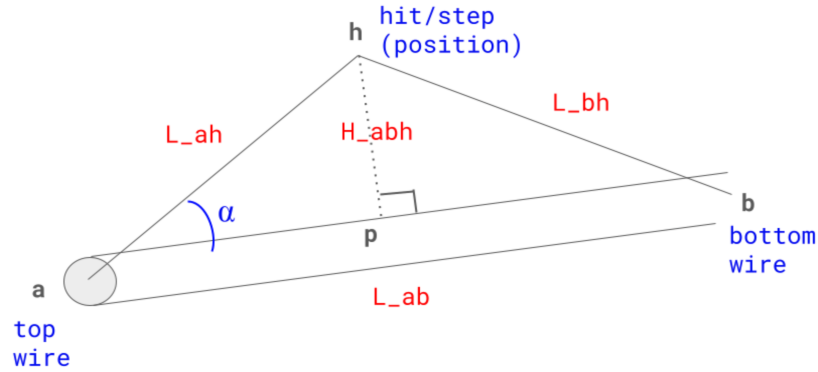
After describing the physical process that leads to the observation of a signal in the ALERT drift chamber, we were able to build a framework capable of generating the characteristic signal of ALERT as a function of certain setting parameters. The results obtained were compared to real signals measured on-beam during a previous study, and we concluded that they were sufficient to begin work on decoding and reconstruction. This is what we have done by implementing a first version of the decoding algorithms. Finally, our thorough understanding of the simulated system enabled us to assess the quality of this decoding.

The implementation of reconstruction algorithms remains to be done. It will be able to rely on the results of the decoding but the frameworks developed during this internship depend on numerous non-optimized parameters. These parameters can only be optimized using real data.

Appendix A

Appendix

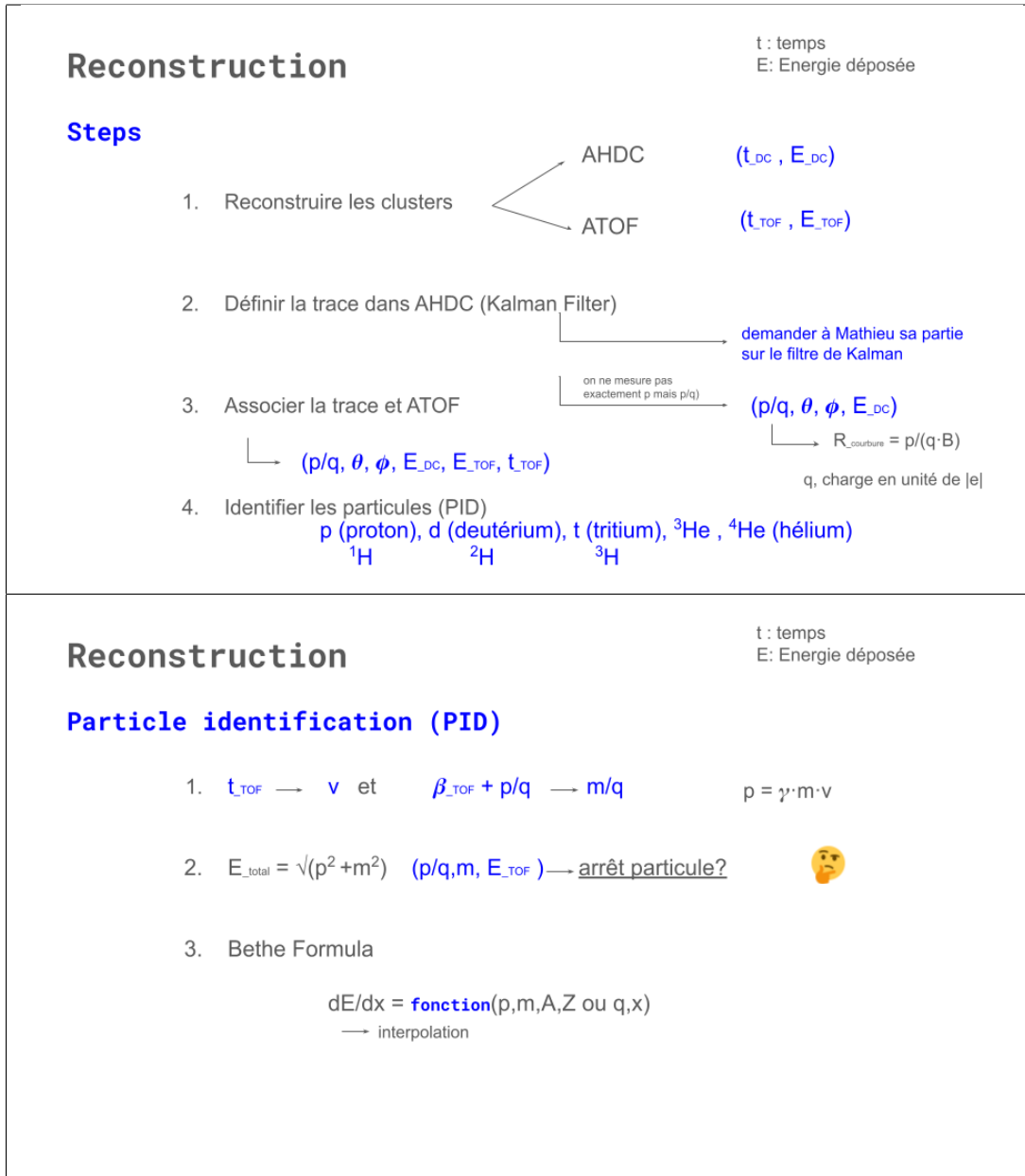
A.1 Doca calculation



Here the doca is defined by H_{abh} .

$$\begin{aligned}
 H_{abh} &= HP \\
 &= AH \sin(\alpha) \\
 &= AH \sqrt{1 - \cos^2(\alpha)} \\
 \overrightarrow{HB}^2 &= \left(\overrightarrow{HA} + \overrightarrow{AB} \right)^2 \\
 &= \overrightarrow{HA}^2 + \overrightarrow{AB}^2 + 2\overrightarrow{HA} \cdot \overrightarrow{AB} \\
 &= \overrightarrow{HA}^2 + \overrightarrow{AB}^2 - 2 \cdot AH \cdot AB \cdot \cos(\alpha) \\
 \cos(\alpha) &= (L_{ah}^2 + L_{ab}^2 - L_{bh}^2) / (2 \cdot L_{ah} \cdot L_{ab})
 \end{aligned} \tag{A.1}$$

A.2 Reconstruction



Bibliography

- [1] IJCLab. *Overview*. URL: <https://www.ijclab.in2p3.fr/en/ijclab-en/overview/>.
- [2] IJCLab. *Organisation chart*. URL: <https://www.ijclab.in2p3.fr/en/ijclab-en/organisation-chart/>.
- [3] Mathieu OUILLON. “Diffusion Compton profondément virtuelle sur le neutron avec l’expérience CLAS12 et le détecteur BONuS12 au laboratoire Jefferson (USA)”. PhD thesis. Particules, Hadrons, Energie et Noyau : Instrumentation, Imagerie, Cosmos et Simulation (PHENIICS), 2024. URL: <https://theses.hal.science/tel-04575566>.
- [4] Mathieu EHRHART. “Nucleon structure studies with CLAS at Jefferson Lab: Deeply virtual Compton Scattering on nitrogen”. PhD thesis. Particules, Hadrons, Energie et Noyau : Instrumentation, Imagerie, Cosmos et Simulation (PHENIICS), 2021. URL: [https://theses.hal.science/tel-03392080/](https://theses.hal.science/tel-03392080).
- [5] L. A. Harland-Lang et al. “Parton distributions in the LHC era: MMHT 2014 PDFs”. In: *arXiv* (2014). URL: <https://arxiv.org/abs/1412.3989>.
- [6] The CLAS Collaboration. “Measurement of deeply virtual Compton scattering off Helium-4 with CLAS at Jefferson Lab”. In: *arXiv* (2021). URL: <https://arxiv.org/abs/2102.07419>.
- [7] A.V. Belitsky and A.V. Radyushkin. “Unraveling hadron structure with generalized parton distributions”. In: *arXiv* (2005). URL: <https://arxiv.org/abs/hep-ph/0504030>.
- [8] Or Hen et al. “Nucleon-Nucleon Correlations, Short-lived Excitations, and the Quarks Within”. In: *arXiv* (2017). URL: <https://arxiv.org/abs/1611.09748>.
- [9] J.J Aubert et al. “The ratio of the nucleon structure functions F2N for iron and deuterium”. In: *Physics Letters B* (2023). URL: [https://doi.org/10.1016/0370-2693\(83\)90437-9](https://doi.org/10.1016/0370-2693(83)90437-9).

- [10] Douglas Higinbotham et al. “The EMC effect still puzzles after 30 years”. In: *CERN Courier* (2013). URL: <https://cerncourier.com/a/the-emc-effect-still-puzzles-after-30-years/>.
- [11] The CLAS Collaboration. “Tagged EMC Measurements on Light Nuclei”. In: *arXiv* (2017). URL: <https://arxiv.org/abs/1708.00891>.
- [12] JLab. *Experimental Nuclear Physics*. URL: <https://www.jlab.org/physics>.
- [13] Douglas Higinbotham. “CEBAF celebrates seven years of physics”. In: *CERN Courier* (2003). URL: <https://cerncourier.com/a/cebaf-celebrates-seven-years-of-physics/>.
- [14] The CLAS Collaboration. “The CLAS12 Spectrometer at Jefferson Laboratory”. In: *Nuclear Instruments and Methods in Physics Research* (2020). URL: <https://doi.org/10.1016/j.nima.2020.163419>.
- [15] The CLAS Collaboration. “Partonic Structure of Light Nuclei”. In: *arXiv* (2017). URL: <https://arxiv.org/abs/1708.00888>.
- [16] Lucien CAUSSE. “Mise au point d’une chambre à dérive stéréo pour l’expérience ALERT au laboratoire Jefferson”. PhD thesis. Particules, Hadrons, Energie et Noyau : Instrumentation, Imagerie, Cosmos et Simulation (PHENIICS), 2021. URL: <https://theses.hal.science/tel-03613763v1>.
- [17] EDINBURGH INSTRUMENTS. *Component Close-Up: Constant Fraction Discrimination*. URL: <https://www.edinst.com/blog/constant-fraction-discrimination/>.

Résumé

Titre : Préparation de l'expérience ALERT au laboratoire Jefferson.

Mots clés : Structure du nucléon, instrumentation, détecteur, simulation

L'expérience ALERT ouvre de nouvelles perspectives pour l'étude de la structure du nucléon à travers des mesures très sophistiquées telles que la diffusion Compton virtuelle profonde (DVCS) ou l'EMC taggée. Ces mesures sont motivées par leur utilité pour extraire les distributions de partons généralisées des nucléons et leur capacité à mettre à l'épreuve les modèles théoriques cherchant à décrire les noyaux en termes de quarks et de gluons. Conçu au IJCLab, le détecteur ALERT est composé d'une chambre à dérive hyperbolique pour le suivi des particules et d'un hodoscope scintillateur pour la mesure du temps de vol.

Un aspect significatif du développement d'ALERT réside dans son logiciel. Pour cela, il était crucial de simuler la réponse du détecteur ALERT lors des mesures en faisceau. En analysant les processus physiques menant à la détection de signaux dans la chambre à dérive d'ALERT, une infrastructure logicielle a été développé pour générer des signaux caractéristiques en fonction de paramètres spécifiques. Ces résultats simulés ont été comparés à des signaux réels mesurés en faisceau lors d'une étude précédente, démontrant leur adéquation pour initier le travail de décodage et de reconstruction. Une version préliminaire des algorithmes de décodage a été mise en œuvre, et la compréhension approfondie du système simulé a permis d'évaluer la qualité de ce décodage. Les infrastructures logicielles développées dépendent de divers paramètres non optimisés, qui pourraient être affinés à l'aide de données réelles pour les opérations d'étalonnage lors de la collecte de données prévue en février 2025.

Abstract

Title : Preparation of the ALERT experiment at Jefferson Lab.

Keywords : Nucleon structure, instrumentation, detector, simulation

The ALERT experiment opens up new ways of investigating the nucleon structure through very sophisticated measurements such as the Deep Virtual Compton Scattering or the Tagged EMC. These measurements are motivated by either their convenience to extract nuclear Generalized Parton Distributions and their ability to challenge theoretical models that try to describe nuclei in terms of quarks and gluons. Designed at IJCLab, the ALERT detector is composed of an hyperbolic drift chamber for particle tracking and a scintillator hodoscope for time-of-flight measurement.

A significant aspect of the ALERT development is its software. To achieve this, simulating the ALERT detector's response during on-beam measurements was crucial. By analyzing the physical processes leading to signal detection in the ALERT drift chamber, a framework was developed to generate characteristic signals based on specific parameters. These simulated results were compared to real on-beam signals from a previous study, demonstrating their adequacy for initiating work on decoding and reconstruction. A preliminary version of decoding algorithms was implemented, and the thorough understanding of the simulated system allowed for an assessment of decoding quality. The frameworks rely on various non-optimized parameters, which could be fine-tuned using real data for calibration during the scheduled February 2025 data collection.